SEISMIC SAFETY ASSESSMENT OF BASE ISOLATED BUILDINGS USING LEAD-RUBBER BEARINGS

by

Hongzhou Zhang

B.Eng., Jilin University, 2014

A THESIS SUBMITTED IN PARTIAL FULFILLMENT OF

THE REQUIREMENTS FOR THE DEGREE OF

MASTER OF APPLIED SCIENCE

in

THE FACULTY OF GRADUATE AND POSTDOCTORAL STUDIES

(Civil Engineering)

THE UNIVERSITY OF BRITISH COLUMBIA

(Vancouver)

April 2018

Abstract

Base isolation using lead-rubber bearing (LRB) has been well-developed and widely-implemented in high seismic zones worldwide. During strong earthquake shaking, LRB is designed to move horizontally and meanwhile carry large axial load. One of the main design challenges is to prevent the LRB from buckling. Although detailed component behavior of LRB under combined axial and shear loads has been well investigated, the seismic performance of base isolated building with LRB has not been systematically examined. In this study, the seismic performances of two prototype buildings, each with different LRB geometric properties, structural periods, and axial loads, were systematically examined. To properly account for the buckling response of the LRB under combined axial and shear loads, robust finite element models of the prototype buildings were developed using the state-of-the-art LRB buckling model implemented in OpenSees. Nonlinear time history analyses were conducted using ground motions selected and scaled based on the 2015 National Building Code of Canada. As shown by the result, when the LRB is designed without accounting the axial and shear interaction, this leads to high probability of failure of the LRB, which can be difficult and expansive to fix. In some situations, this might lead to the collapse of the base isolated building. To mitigate the failed probability of the LRB during strong earthquake shaking, a simple amplification factor of 2.5 is proposed to amplify the design axial load calculated from the combined gravity and earthquake loads when the coupled axial and shear interaction of LRB is not explicitly modeled.

Lay Summary

Lead-rubber bearing (LRB) has been implemented worldwide as an effective seismic isolation device to protect the buildings from earthquake shaking. This thesis aims to study the failure behavior of buildings isolated using LRBs based on advanced numerical modeling techniques. Two prototype buildings in Vancouver, BC, Canada were used as the case study. The buildings were designed based on different combinations of parameters, and analyzed numerically using earthquake records selected based on the 2015 National Building Code of Canada. An amplification factor was proposed for practical design in order to guarantee the low probability of LRB failure under severe earthquakes.

Preface

This thesis is the original, independent work of Hongzhou Zhang. The author was responsible for the literature review, model development, computational analysis, data processing, and results presentation. The thesis was drafted by the author and revised based on the comments of Professor Tony Yang, at the University of British Columbia.

Table of Contents

List of Tables

List of Figures

List of Symbols

K_V: vertical stiffness

A_b: bonded rubber area

E_c: compression modulus

T_r: total rubber thickness

u_h: shear deformation

r: radius of gyration of the bonded rubber area

K_{V0}: axial compressive stiffness at zero shear deformation

K_H: horizontal stiffness

K_{H0}: horizontal stiffness at zero axial load

G_r: rubber shear modulus

P: axial load

P_{cr}: critical buckling load

P_{cr0}: critical buckling load of LRB under zero horizontal displacement

A_S: shear area including the effect of the rigidity of steel shims

I_S: moment of inertia including the effect of the rigidity of steel shims

I: moment of inertia of the area of bonded rubber

h: height of LRB including rubber layers and steel shims

E_r: rotational modulus

S: shape factor of single rubber layer

F: diameter modification factor

K: bulk modulus of rubber

S: shape factor of single rubber layer

F: diameter modification factor

K: bulk modulus of rubber

D_2: diameter of LRB

D_1: diameter of lead core

t_r: single rubber layer thickness

A_r: reduced area

Q: characteristic strength

K_1: the initial stiffness

K_2: post-elastic stiffness

D_{max}: maximum displacement

S_a: spectral acceleration

S_d: spectral displacement

ξ_{eff}: equivalent damping ratio

B: damping reduction factor

W_D: energy dissipated per hysteresis cycle

K_{eff}: effective stiffness

F_{yl}: yield strength of lead

D_{Tmax}: maximum total displacement

e: actual eccentricity plus 5% accidental eccentricity

T_p: post-elastic period of isolated building

T_f: fixed-base period

W: building weight

F_x: distributed base shear at level x

V_s: base shear for the superstructure

V_u: link shear

D: dead load

L: live load

S: snow load

E: earthquake load

T_R: period range for ground motion selection

T_{RS}: scenario specific period range

List of Abbreviations

AASHTO: American Association of State Highway and Transportation Officials

ASCE: American Society of Civil Engineers

CSA: Canadian Standards Association

CSM: capacity spectrum method

EBF: eccentrically braced frame

LRB: lead-rubber bearing

MCE: maximum considered earthquake

NBCC: National Building Code of Canada

PEER: Pacific Earthquake Engineering Research Center

PSHA: probabilistic seismic hazard analysis

SDOF: single degree of freedom

SFRS: seismic force resisting system

Acknowledgements

First, I would like to express my sincere gratitude to my supervisor, Professor Tony Yang. His patience, motivation, and immense knowledge have guided me in exploring the world of innovative engineering technologies. Without his selfless support and insightful advice, this research would not have been possible. I also would like to thank Prof. Wei Guo for reviewing my thesis and providing valuable advice.

I would like to offer my thanks to my research colleagues, Yuanjie Li, Dorian Tung, and Lisa Tobber, for their valuable guidance and advice which helped me with the technologies I had needed to investigate for my research. My gratitude also extends to my other friends in the department including Dongbin Zhang, Tianyi Li, Yuxin Pan, and Tianxiang Li for their help with my studies.

My deepest gratitude goes to my parents for their unconditional support and unwavering belief in me. Above all, I would like to thank my wife, Mi Zhou, for her endless love and support.

Dedication

This thesis is dedicated to my parents and brother.

Chapter 1: Introduction

1.1 Seismic Isolation

Seismic isolation is a well-developed and widely-implemented technique used to mitigate structural and non-structural damage under severe earthquake shaking. This technique decouples the superstructure from the substructure by interposing components with low horizontal stiffness under the superstructure. The soft layer (i.e., the isolation system) results in a lengthened fundamental period as compared with the period of the same building with fixed base, significantly reducing the seismic force transmitted to the superstructure. Some isolation systems also provide additional damping to the structure, thus further reducing the seismic demand. The effect of seismic isolation can be simply illustrated in Figure 1.1, where the spectral acceleration (S_a) decreases with the increase of the period (T). Compared to a conventional fixed-base building, the superstructure of an isolated building can remain elastic during earthquakes due to its reduced demand. The response of an isolated low- or mid-rise building under horizontal ground motion is dominated by the first dynamic mode, where its lateral deformation is concentrated in the isolated system, causing the superstructure to move like a rigid body. Another benefit of seismic isolation is that the reduced acceleration of the superstructure will protect the building's non-structural components. Isolated buildings' superior seismic performance allows them to achieve full operation during severe earthquakes.

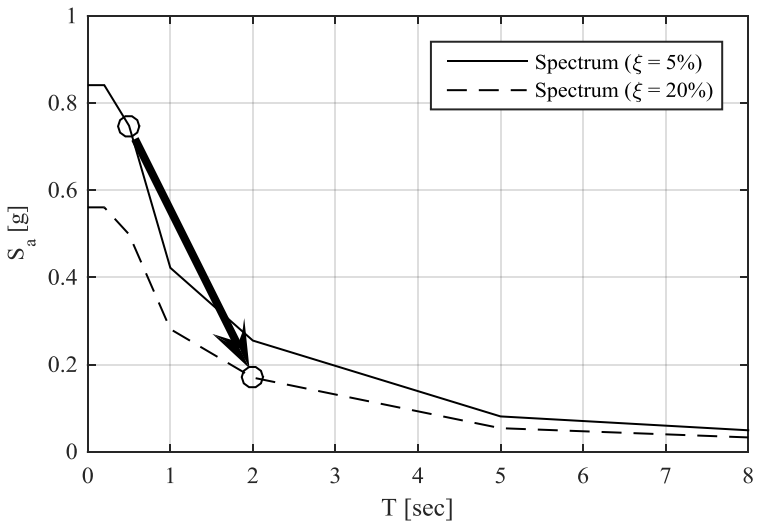

Figure 1.1 The effect of period shift and damping of seismic isolation

Seismic isolation has been studied intensively and implemented in numerous bridges, buildings, and infrastructures over the last three decades. A variety of seismic isolation hardware types have been developed, and these can be classified into two main categories: elastomeric bearings and sliding bearings [1]. Elastomeric bearings are made from laminated rubber layers and steel shims. The configurations of elastomeric bearings allow them to move horizontally with low stiffness while possessing a substantial vertical load carrying ability sufficient to support the superstructure. The rubber used in this type of bearing can be either low- or high-damping. Invented in New Zealand in 1976 [2], the lead-rubber bearing (LRB) have been extensively implemented throughout the world. LRBs differ from low-damping rubber bearings only by the lead core inserted in their central holes. This lead core provides stable energy dissipation following its yielding during earthquakes. Figure 1.2 reveals the configuration of low-damping rubber bearing and lead-rubber bearing. The hysteresis behavior of diverse elastomeric bearings is shown in

Figure 1.3. Compared to low- and high-damping rubber bearings, lead-rubber bearings have a more stable bilinear hysteresis behavior able to provide predictable damping.

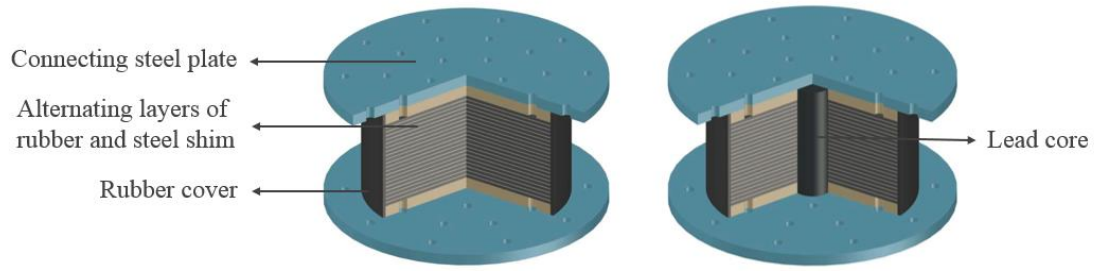

Figure 1.2 Low-damping rubber bearing and lead-rubber bearing

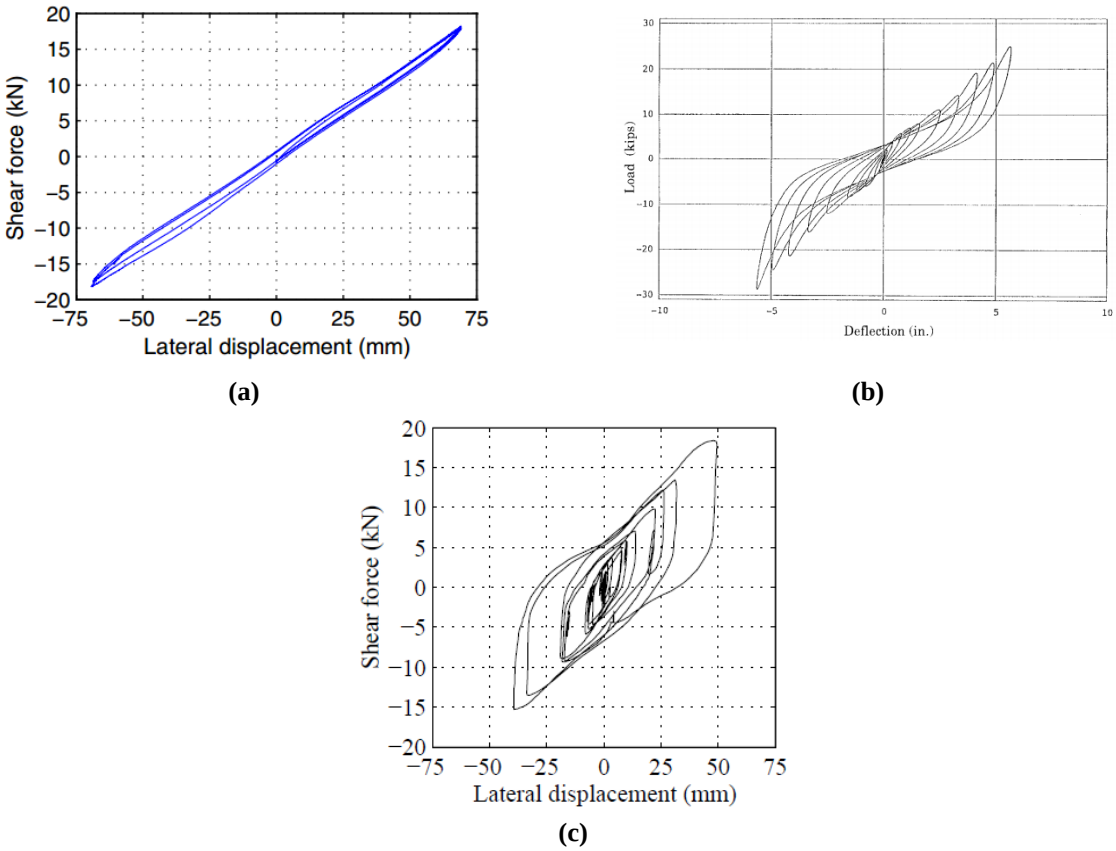

(a) **(b)**

(c)

Figure 1.3 The different hysteresis behaviors of elastomeric bearings (a) Low-damping rubber bearing [3]; (b) High-damping rubber bearing [4]; (c) Lead-rubber bearing [5]

The sliding bearing is a frictional isolation device utilizing the friction between the slider and sliding surface as demonstrated in Figure 1.4. The geometry of the sliding surface in the friction pendulum system can provide a restoring force and stable bilinear hysteresis behavior during earthquakes. An improved sliding bearing is called triple pendulum bearing as shown in Figure 1.5. The triple pendulum system has multi-stage behavior where different stiffness and damping ratio can be achieved at different displacement levels. This type of bearing can be designed to satisfy different performance targets based on small, moderate, and severe earthquakes.

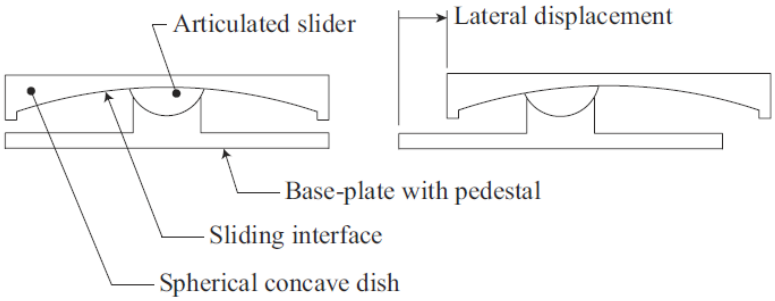

Figure 1.4 Friction pendulum system [1]

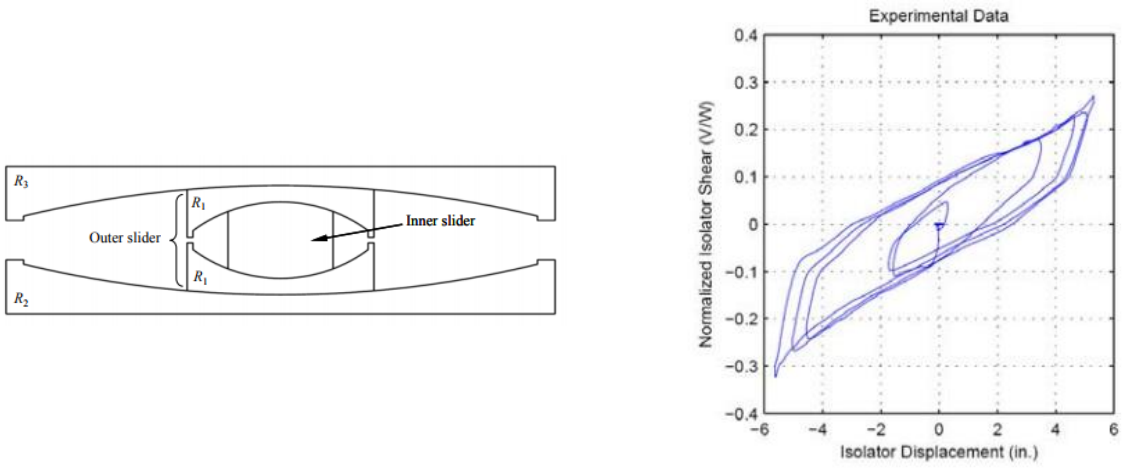

Figure 1.5 Triple pendulum bearing [6]

The effectiveness of seismic isolation has been examined by the performance of isolated buildings during earthquakes. A well-known example is the base-isolated computer center of the Ministry of Post and Telecommunications in Japan. The isolation system of the building was implemented using a combination of low-damping rubber bearings, lead-rubber bearings, and steel dampers. During the 1995 Hanshin-Awaji Earthquake, the peak acceleration experienced by the superstructure of the computer center were reduced to about 1/4 and 1/3, respectively, in the two horizontal directions of that on the foundation. The excellent performance of the isolated buildings showed the effectiveness of seismic isolation. After 1995, the number of isolated buildings in Japan increased dramatically [7]. As a further example, the USC Hospital in Los Angeles performed well during the strong earthquake ground shaking of the 1994 Northridge Earthquake. The drift ratios of the superstructure were less than 10% of the limit, and the building was undamaged [8]. Additionally, the Japan Society of Seismic Isolation collected the response data of isolated buildings in Japan during and after the 2011 Tohoku Earthquake. The records show that all isolated buildings remained undamaged and that their occupancy continued after the earthquake.

1.2 Stability of LRB

During earthquakes, elastomeric bearings experience large degrees of horizontal deformation to reduce the response of the superstructure as caused by their low stiffness levels. However, these large displacements are always accompanied by high compressive axial loads resulting from the superstructures' gravity loads and the seismic overturning forces, which cause buckling failure in the elastomeric bearing. Figure 1.6 illustrates buckling failure of an elastomeric bearing tested by

Sanchez *et al*. [9]. Due to P-Δ effect, the buckling load capacity of the elastomeric bearing decreases with the increase in shear deformation. When the buckling occurs, the bearing will lose its shear and axial resistance. Isolation systems are normally placed at the base or lower levels of buildings and the axial loads transmitted to them are significant. In such situations, the buckling of the isolators during earthquakes will cause severe damage to buildings and immense life losses. Therefore, the design of elastomeric bearings to prevent buckling under severe earthquakes is crucial.

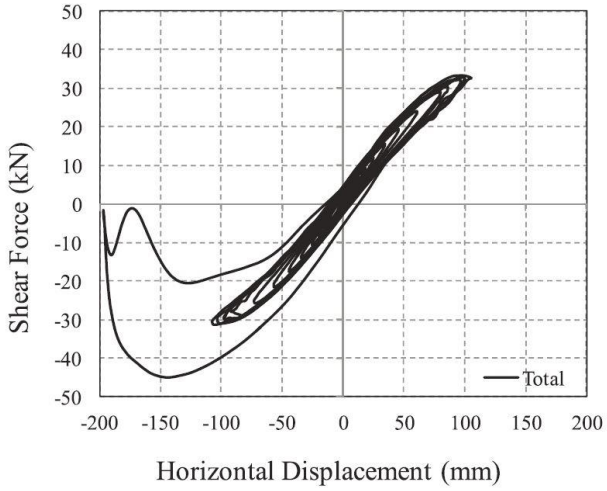

Figure 1.6 The dynamic stability test hysteresis loop of an elastomeric bearing [9]

As a type of elastomeric bearing, the LRB is facing the same challenge of buckling failure under large shear deformation. The theory to calculate the buckling load of LRBs can be dated back to the works done by Haringx [10] in the 1960s. In this study, the influence of the axial force on the horizontal stiffness and the buckling load of a slender elastic column under combined flexural and shear deformation was derived analytically. Gent [11] applied Haringx's theory in predicting the critical buckling load of elastomeric bearings and verified his theory with experimental tests. The

results revealed that Haringx's theory can be used to model the buckling behavior of elastomeric bearings under combined axial and shear loads well. Koh and Kelly [12, 13] further improved the Haringx's theory and developed a detailed viscoelastic model for elastomeric bearings for dynamic application. They have conducted detailed numerical simulation and verified against experimental dynamic tests. The result shows the detailed viscoelastic model can accurately model the dynamic behavior of elastomeric bearings. However, the detailed viscoelastic model was too complicated for typical structural engineering applications. For this reason, Koh and Kelly [14] developed a simplified two-spring model to simulate the stability effects of elastomeric bearings. The two-spring model provided close approximation to the detailed model and it was validated using experimental tests [14, 15]. Based on the theory developed, the two-spring model was not able to simulate the load capacity of the LRBs under large horizontal deformation. To overcome this inefficiency, Buckle and Liu [3, 16] developed the overlapping area method to calculate the axial capacity of LRBs under large horizontal deformation. According experimental tests, this method provided a conservative prediction of the buckling load [3, 16].

1.3 Design Provisions

Many of the building and bridge codes worldwide have considered the stability of isolators during the seismic design. The American building code ASCE-7 [17] and bridge code AASHTO [18] have different clauses for the vertical load stability of isolators (clause 17.2.4.6 and 12.3, respectively). ASCE-7 indicates that the isolator should be designed to resist combined axial load (from dead, live and earthquake) when the shear deformation reached the maximum total displacement. The AASHTO code presents more stringent requirements, whereby the isolators are

required to satisfy the following two criteria: (1) That the axial capacity of the isolator at zero shear deformation shall have a compression capacity larger than three times the sum of the unfactored dead and live loads; and (2) That the isolator shall be designed to resist a combined dead, live, and earthquake loads, at the amplified maximum total displacement. The Canadian building code [19] and bridge code [20] have similar requirement, where the isolator shall has sufficient load carrying capacity at the target shear deformation. The Chinese code [21], on the other hand, considers the stability issue by limiting the compressive pressure and lateral deformation on each isolator.

1.4 Motivation and Objectives

One of the design challenges of LRB is the ability to carry axial load under large shear deformation, where the LRB could buckle. LRBs are usually installed at the base of a building, hence the buckling failure of LRBs could result in difficult structural repair and hefty financial losses. Therefore, it is crucial to mitigate the buckling failure of LRBs under the maximum considered earthquake (MCE) shaking.

Typically speaking, the force-deformation response in shear direction of the LRB is modeled using a simple bilinear model without considering the axial and shear coupling effects. According to the previous research, the axial stiffness of the LRB decreases with the increase of shear deformation. Apart from that, the axial force will result in the reduction of shear stiffness [14]. Therefore, the simple bilinear model will overestimate the behavior of the LRB and ignore the potential buckling failure. For overcoming this deficiency, Kumar developed a state-of-the-art 3D LRB model [22]. This model adopted the algorithm of the two-spring model and overlapping area method to

simulate the axial and shear coupling as well as buckling effect of LRBs. Although detailed component behavior of LRB under combined axial and shear loads has been well investigated, the seismic performance of base isolated building with LRB has not been systematically examined.

The first objective of this research is to systematically study the seismic performance of building isolated by LRBs with different LRB geometric properties, structural periods, and axial loads. The study is based on the nonlinear time history analyses on robust finite element models developed using the advanced LRB buckling model in OpenSees. The second objective is to propose a simple amplification factor to amplify the design axial load of LRB for practical design when the coupled axial and shear interaction of LRB is not explicitly modeled. The amplification factor aims at mitigating the probability of LRB buckling failure for isolated buildings under severe earthquake shaking.

1.5 Scope of the Work

The scope of work for this study is as follows:

1) Review the theories on the mathematical approaches to the LRB buckling effect.
2) Present a design procedure for seismic isolation systems with bilinear behavior according to the capacity spectrum method.
3) Develop a design method to calculate the LRBs' geometry properties in accordance with the determined bilinear model and target axial capacity when the LRBs are subjected to the maximum total displacement.

4) Implement the design procedure in designing two prototype buildings isolated by LRBs. Each building will be designed according to different groups of parameters including its target period, the single rubber layer thickness, and the axial capacity.
5) Develop detailed finite element models of the prototype buildings in OpenSees [23] utilizing the advanced 3D mechanical model for LRBs, "*LeadRubberX*" [22], which takes LRB buckling behavior into consideration.
6) Conduct nonlinear time history analyses on the developed models using ground motions selected and scaled according to the 2015 National Building Code of Canada (NBCC). Identify failure events resulted by the buckling of LRB.
7) Summarize the results and provide recommendations.

1.6 The Organization of this Thesis

Chapter 2 of this thesis reviewed the theories on the mechanical properties of LRBs, including the coupled vertical-horizontal response and the buckling effect. The numerical model used in this study was also introduced. The approach to design the bilinear model for the LRB system according to the target period and damping ratio is explained in Chapter 3. In Chapter 4, the design procedure to determine the geometric properties of the LRBs based on the bilinear model and axial capacity, is specified. Chapter 5 introduces the seismic hazard in Vancouver, BC, Canada, and provides ground motion selection for the analysis based on hazard analysis. In Chapter 5, two prototype buildings for location at Vancouver City Hall are designed using LRBs at their base according to different target periods, single rubber layer thicknesses, and axial capacity. The time

history analysis results are summarized and presented in Chapter 6. Finally, conclusions are drawn in Chapter 7.

Chapter 2: Mechanical Behavior of LRBs

This chapter will introduce the well-established theory on the mechanical behavior of lead-rubber bearings. The coupling of horizontal and vertical responses and the calculation of the buckling load under large shear deformation levels have already been discussed. However, the nonlinear behavior of LRBs under tension is not the focus of this study, and has not been included in this chapter. A robust numerical model that includes all theories on the mechanical behavior of LRBs is also introduced. This model is applied in this study to model LRBs and account for buckling behavior.

2.1 Interactions Between Horizontal and Vertical Directions

The horizontal and vertical responses of LRBs are coupled. This effect can be considered from two aspects: the influence of shear stiffness on axial loads and the effects of axial stiffness on shear displacements. The two-spring model developed by Koh and Kelly [14] was a simplified model using two linear springs to account for the shear and flexural behavior of elastomeric bearings as shown in Figure 2.1. The two-spring model was found to provide a close approximation to the previously developed detailed model and was validated using experimental tests [14, 15].

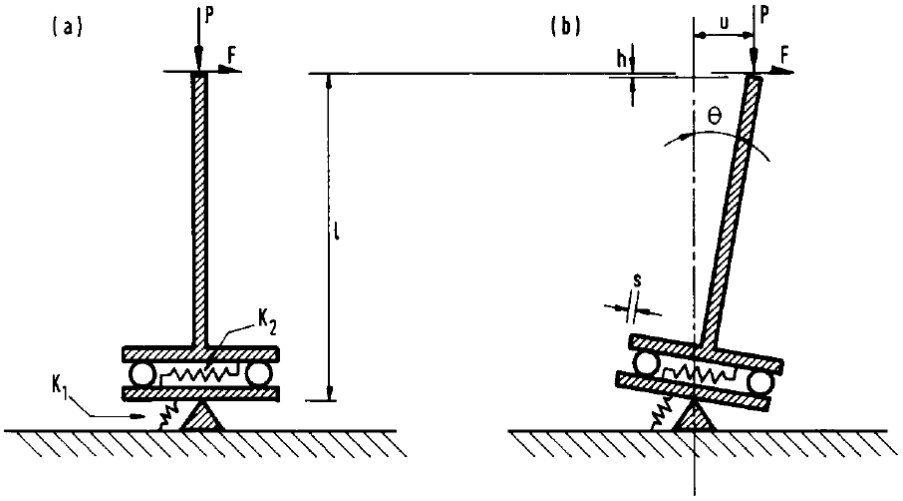

Figure 2.1 A simple mechanical model for elastomeric bearings [14]

The vertical stiffness of the LRB can be derived from the two-spring model as follows:

$$K_V = \frac{A_b E_c}{T_r}\left[1+\frac{3}{\pi^2}\left(\frac{u_h}{r}\right)^2\right]^{-1} = K_{V0}\left[1+\frac{3}{\pi^2}\left(\frac{u_h}{r}\right)^2\right]^{-1} \quad 2.1$$

where

A_b = bonded rubber area

E_c = compression modulus of the bearing

T_r = total rubber thickness

u_h = shear deformation

r = radius of gyration of the bonded rubber area

K_{V0} = axial compressive stiffness at zero shear deformation

The horizontal stiffness can be expressed as a function of the axial load and critical buckling load:

$$K_H = \frac{G_r A_b}{T_r}\left[1 - \left(\frac{P}{P_{cr}}\right)^2\right] = K_{H0}\left[1 - \left(\frac{P}{P_{cr}}\right)^2\right] \quad 2.2$$

where

G_r = rubber shear modulus

P = axial load

P_{cr} = critical buckling load

K_{H0} = horizontal stiffness at the zero axial load

2.2 Buckling without Shear Deformation

The critical buckling load of an LRB without horizontal displacement can be derived from the two-spring model as [4]:

$$P_{cr0} = \sqrt{P_S P_E} \quad 2.3$$

where P_E and P_S are given by:

$$P_E = \frac{\pi^2 E_r I_S}{h^2} \quad 2.4$$

$$P_S = G_r A_S \quad 2.5$$

where A_S and I_S are the shear area and moment of inertia including the effect of the rigidity of the steel shims, and are calculated as:

$$A_S = A_b \frac{h}{T_r} \quad 2.6$$

$$I_S = I \frac{h}{T_r} \quad 2.7$$

where

I = moment of inertia of the area of bonded rubber

h = height of the LRB including its rubber layers and steel shims

E_r = rotational modulus of the bearing

E_r is given as $E_c/3$ for circular and spare bearings, and where E_c is provided as:

$$E_c = \left(\frac{1}{6G_r S^2 F} + \frac{4}{3K}\right)^{-1} \quad 2.8$$

where

S = shape factor of a single rubber layer

F = diameter modification factor

K = bulk modulus of rubber

The geometric properties mentioned above are derived as follows for a circular LRB:

$$S = \frac{D_2 - D_1}{4t_r} \quad 2.9$$

$$F = \frac{d^2 + 1}{(d-1)^2} - \frac{1 + d}{(1-d)\ln(d)} \quad 2.10$$

$$d = \frac{D_2}{D_1} \quad 2.11$$

$$I = \frac{\pi\left({D_2}^4 - {D_1}^4\right)}{64} \quad 2.12$$

$$A_b = \frac{\pi\left({D_2}^2 - {D_1}^2\right)}{4} \quad 2.13$$

$$r = \sqrt{\frac{I}{A_b}} \quad 2.14$$

where

D_2 = diameter of the LRB

D_1 = diameter of the lead core

t_r = single rubber layer thickness

2.3 Buckling with Shear Deformation

When the LRB is subjected to shear displacement u_h, the critical buckling load is reduced. The reduced buckling load is accounted for by the overlapping area method developed by Buckle and Liu [16]. This method calculates the reduced buckling load based on the overlapping area between the upper- and lowermost layers of the bearing under shear deformation, and provides a conservative prediction of the buckling load [3, 16]. The reduced buckling load of an LRB under shear deformation is given as:

$$P_{cr} = P_{cr0}\frac{A_r}{A_b} \tag{2.15}$$

where A_r is the reduced area as shown in Figure 2.2 and is calculated as:

$$A_r = \frac{{D_2}^2}{4}(\varphi - \sin\varphi) \tag{2.16}$$

$$\varphi = 2\cos^{-1}\left(\frac{u_h}{D_2}\right) \tag{2.17}$$

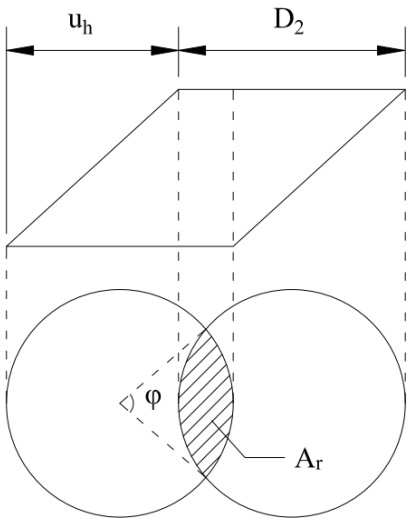

Figure 2.2 Overlapping area method

However, LRBs will not lose their stability when the overlapping area is equal to zero, as suggested by experimental tests [3, 9, 15]. A piecewise function of LRBs' reduced critical buckling load was proposed by Warn *et al*. [15], and is given as:

$$P_{cr} = \begin{cases} P_{cr0}\dfrac{A_r}{A_b} & \left(\dfrac{A_r}{A_b} \geq 0.2\right) \\ 0.2P_{cr0} & \left(\dfrac{A_r}{A_b} < 0.2\right) \end{cases} \qquad 2.18$$

2.4 Advanced Numerical Model

The mathematical approach to considering LRBs' mechanical properties has been implemented in OpenSees by Kumar [22-24]. The algorithm was programmed in the element known as *LeadRubberX* in OpenSees. This three-dimensional element possesses two nodes and 12 degrees of freedom. The physical model of this element is shown in Figure 2.3. This robust numerical model has been validated by experimental tests [24].

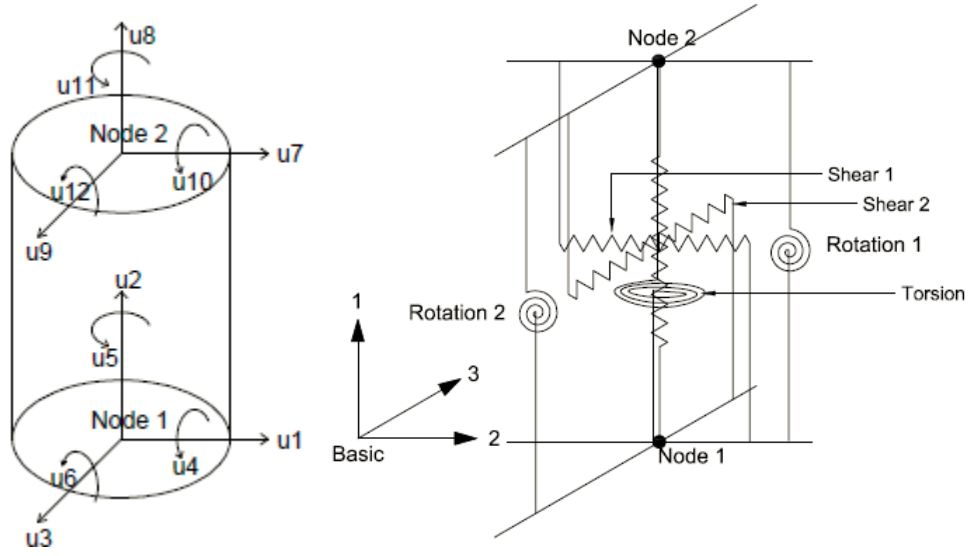

Figure 2.3 Physical model of *LeadRubberX*

This numerical model includes various LRB mechanical behavior patterns, such as coupled shear and axial directions, varying buckling load, and nonlinear in tension. The inputs of the model require only a knowledge of the LRBs' material and geometric properties. Figure 2.4 shows the input needed to define a *LeadRubberX* element. The coupling of the two horizontal directions is accounted for by a coupled bidirectional model, while the coupling of vertical and horizontal directions is accounted indirectly using the coupling equations in Section 2.1. The buckling effects summarized in Sections 2.2 and 2.3 are explicitly considered in this model. The recorder for this element can register the instantaneous values of the critical buckling load, which are displacement-dependent. In the numerical analysis for this study, the LRBs' recorded buckling loads were checked at every time series step and then compared with the real-time axial loads in order to recognize failure events. The analysis was stopped with any exceeding of the buckling load, thus conserving a large amount of time in the analysis process.

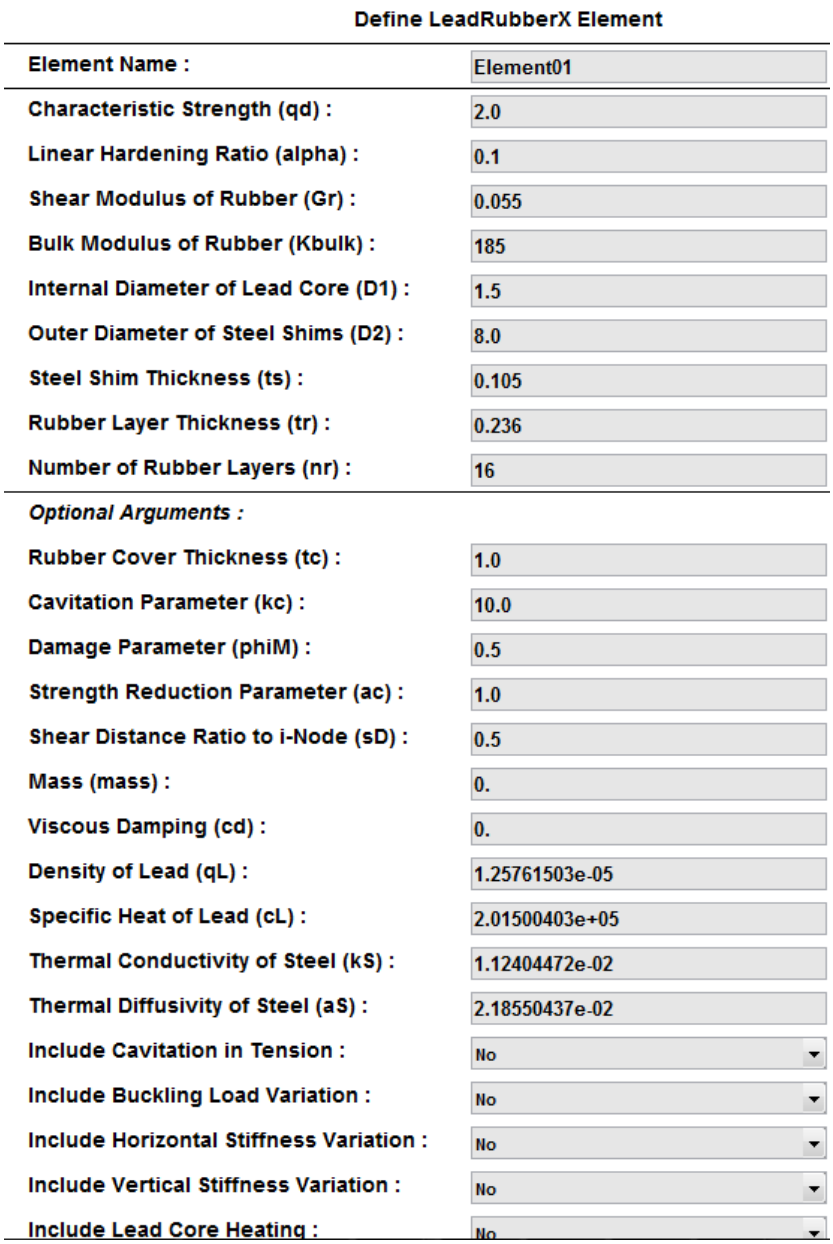

Figure 2.4 Example inputs for *LeadRubberX*

Chapter 3: Design Procedure for LRB Isolated Buildings

This chapter begins by introducing the capacity spectrum method (CSM) for designing the LRBs' bilinear model parameters using the target spectrum. The procedure uses the assumed target damping ratio of the isolation system and isolated fundamental period as inputs, and calculates the key parameters of the bilinear model utilizing an iterative process. The second part of this chapter presents a procedure used to determine the geometry of an LRB required to achieve the designed bilinear model and the target axial capacity under the maximum total displacement.

3.1 Capacity Spectrum Method

The capacity spectrum method (CSM) is a graphical approach to compare the structural capacity with the seismic demand on the structure as illustrated in Figure 3.1 [25]. In this method, the capacity of a structure can be generated by a force-displacement relationship. Then the structure can be idealized to an equivalent Single-Degree-Of-Freedom (SDOF) system by converting the base shear and the roof displacement of the structure to spectral acceleration and spectral displacement, respectively. The seismic demand is defined by a damped spectral displacement – spectral acceleration plot. An intersection point can be found when the capacity of the structure and the seismic demand are plotted together, which provides an inelastic strength and deformation demand for the structure. The CSM provides a simple way to design an inelastic structure and a visual assessment of how the structure will perform under earthquake shaking.

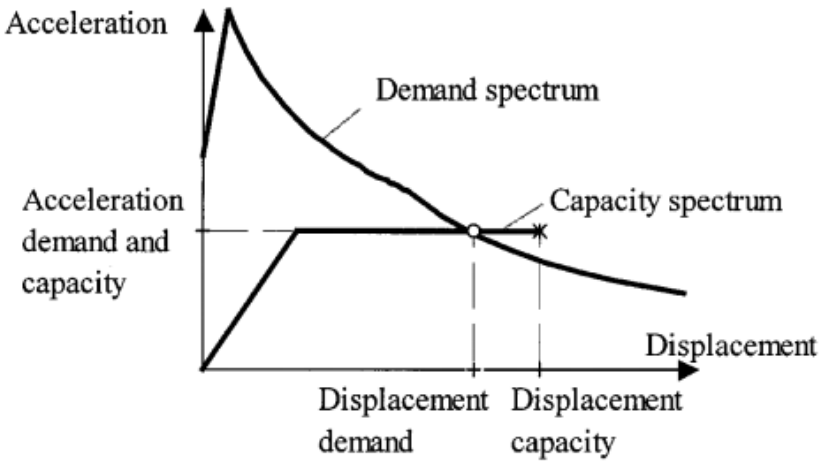

Figure 3.1 Capacity spectrum method [25]

3.2 Bilinear Model Design

Without considering the axial and shear coupling behavior of the LRB, the seismic response of the base isolated building with LRB can be designed with bilinear model using CSM. With the location of the prototype building selected, the seismic demand of the prototype site can be represented using the demand curve as shown in Figure 3.2. The vertical axis is represented using spectral acceleration (S_a) multiplied by the mass of the structure, while the horizontal axis is represented using the spectral displacement (S_d). The response of a low- or mid-rise isolated building is dominant by the fundamental structural period because of the low stiffness of isolation system. Therefore, in the capacity spectrum method, an isolated building can be idealized as a single-degree-of-freedom structure with the mass of the superstructure and the stiffness of the isolation system. Because the vertical axis represents the base shear and the horizontal axis represents the isolator deformation, the bilinear response of the LRB (known as the capacity curve) and the demand curve can be plotted together as shown in Figure 3.2.

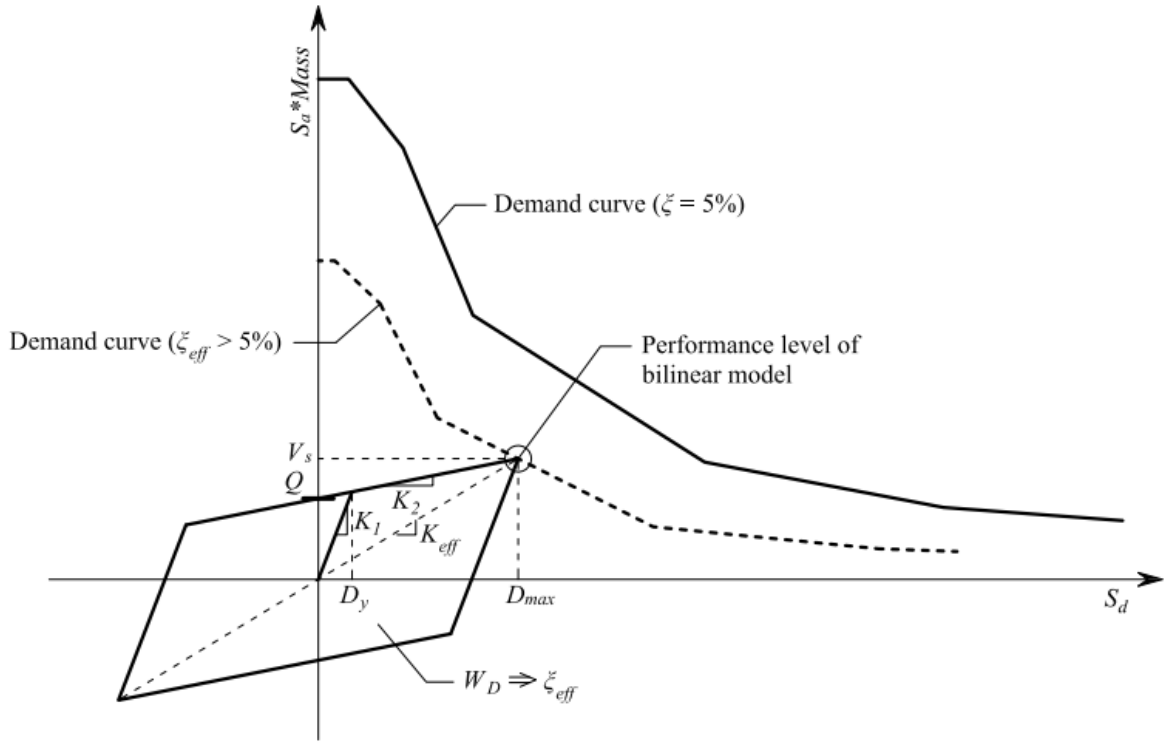

Figure 3.2 Bilinear model vs S_a*Mass - S_d plot

A bilinear model can be fully characterized by four key parameters: (1) the characteristic strength (Q); (2) the initial stiffness (K_1); (3) the post-elastic stiffness (K_2); and (4) the maximum displacement (D_{max}) [26] which is shown in Figure 3.2. The procedure of bilinear model design starts with the assumed target fundamental period (T_p) of the isolated building computed by the post-elastic stiffness of the isolation system (according to NBCC [19]) and the target equivalent viscous damping ratio (ξ_{eff}) of the isolation system.

Based on ξ_{eff}, the demand curve is reduced from the 5% damped demand curve using:

$$S_a(\xi_{eff}) = \frac{S_a(5\%)}{B} \qquad 3.1$$

$$S_d(\xi_{eff}) = \frac{S_d(5\%)}{B} \quad (3.2)$$

where B is the damping reduction factor listed in

Table 3.1.

Table 3.1 Damping reduction factor [17]

Equivalent viscous damping ratio, ξ_{eff}	B
≤ 2%	0.8
5%	1.0
10%	1.2
20%	1.5
30%	1.7
40%	1.9
≥ 50%	2.0

Based on T_p, K_2 can be determined by T_p and the weight of the superstructure (W):

$$K_2 = \left(\frac{2\pi}{T_p}\right)^2 \frac{W}{g} \quad (3.3)$$

As an approximate rule of thumb, K_1 is taken as $10K_2$. With a trial of Q value, D_{max} can be determined by finding the intersection point of the capacity curve (bilinear line) and the reduced demand curve. Equation 3.4 - 3.7 show the derivation of D_y, K_{eff}, and W_D (energy dissipated per cycle) as functions of the key parameters.

$$D_y = \frac{Q}{K_1 - K_2} \quad (3.4)$$

$$K_{eff} = K_2 + \frac{Q}{D_{max}} \quad (3.5)$$

$$W_D = 2\pi\xi_{eff} K_{eff} {D_{max}}^2 \quad (3.6)$$

$$Q = \frac{W_D}{4(D_{max} - D_y)} \quad 3.7$$

However, Q can be derived using Equation 3.7 which is coupled with the previous equations. Therefore, an iterative procedure (illustrated in Figure 3.3) is necessary to calculate the bilinear design parameters. In this procedure, the target post-elastic period and damping ratio are considered as inputs. Then, the demand curve can be determined by reducing the 5% damped demand curve based on the target damping ratio. Using the initialized Q, the other bilinear model parameters can be calculated. However, another Q is also computed according to the derived parameters. If the Q is not closed enough to the value in the previous step, the procedure will be recalculated based on the new value of Q. The iterative procedure will provide the final solution if the results between two successive steps are sufficiently close in value.

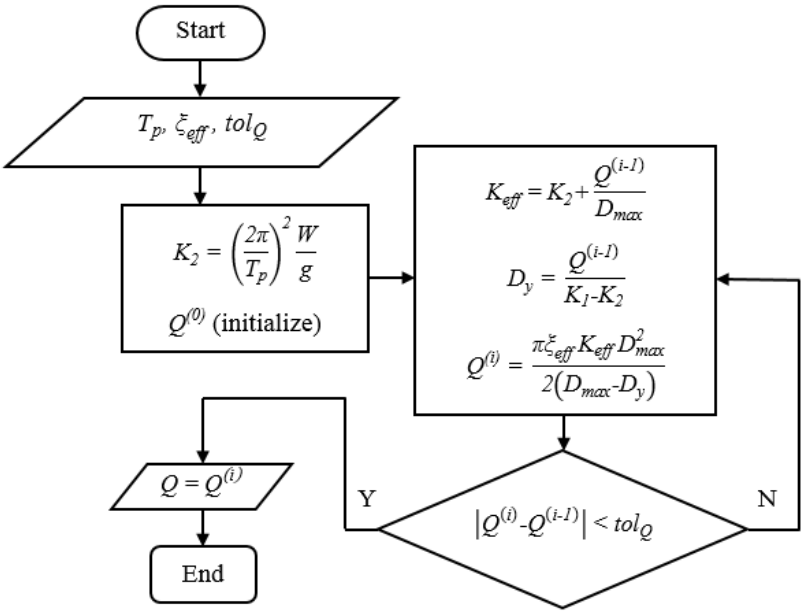

Figure 3.3 The iterative design procedure for bilinear models

In this study, the target damping ratio is selected such that the base shear transmitted to the superstructure is minimized. Figure 3.4 shows an illustration of damping optimization, where the three bilinear models share the same isolation period but different damping ratio. In this case, system B has the lowest base shear; hence, the corresponding damping ratio is selected as the most optimal one.

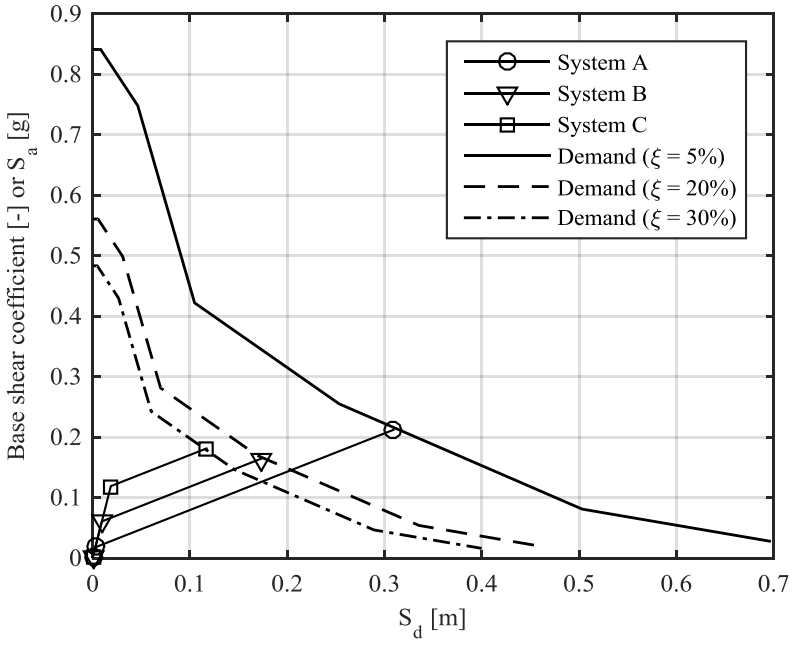

Figure 3.4 Damping ratio optimization

3.3 LRB Design

The parameters that define an LRB are: 1) the material properties of rubber, such as shear modulus of rubber (G_r) and bulk modulus of rubber (K); 2) shear yield strength of lead (F_{yl}); 3) the geometric properties of the LRB, including the lead diameter (D_1), the total diameter (D_2), the steel shim thickness (t_s), the single rubber layer thickness (t_r), and the number of rubber layers (n_r). Once the bilinear model of an LRB has been defined, different combinations of geometric properties can

result in the same bilinear behavior, but with different axial capacity. In this study, G_r, K, t_s, and F_{yl} are assumed to be constants and the influence of the t_r and n_r on the buckling capacity of the LRB is analyzed.

For a given t_r and n_r, the lead diameter (D_1), the total rubber thickness (T_r), the bonded rubber area (A_b), and total diameter (D_2) can be calculated based on the bilinear model parameters using the following equations:

$$D_1 = \sqrt{\frac{4Q}{\pi F_{yl}}} \tag{3.8}$$

$$T_r = n_r t_r \tag{3.9}$$

$$A_b = \frac{T_r K_2}{G_r} \tag{3.10}$$

$$D_2 = \sqrt{\frac{4A_b}{\pi} + {D_1}^2} \tag{3.11}$$

Once the geometry of an LRB has been defined, the buckling load of the LRB with shear deformation can be calculated according to the procedure shown in Chapter 2. It should be noted that the capacity of LRB should be calculated as the critical buckling load under D_{Tmax}, which is the maximum total displacement of the LRB considering the torsional response of the building as given by [4]:

$$D_{Tmax} = D_{max}\left(1 + y\frac{12e}{b^2 + d^2}\right) \tag{3.12}$$

where

e = actual eccentricity plus 5% accidental eccentricity

y = distance to a corner perpendicular to the direction of the seismic loading

b, d = dimensions of the building plan

The equation is generated based on the assumption that the seismic load $K_{eff}D$ is acting on the mass center which has a distance from the center of stiffness of e as shown in Figure 3.5. For a $b \times d$ rectangular plan, assuming that the isolators are evenly distributed at the base of the building, the torsional stiffness of the isolation system is given as $K_{eff}(b^2 + d^2) / 12$. The corresponding rotation caused by the seismic load is calculated as:

$$\theta = \frac{K_{eff}De}{K_{eff}\left(\frac{b^2 + d^2}{12}\right)} = \frac{12De}{b^2 + d^2} \tag{3.13}$$

Thus, the additional displacement resulting from the torsional effect is given by:

$$\frac{12De}{b^2 + d^2}y \tag{3.14}$$

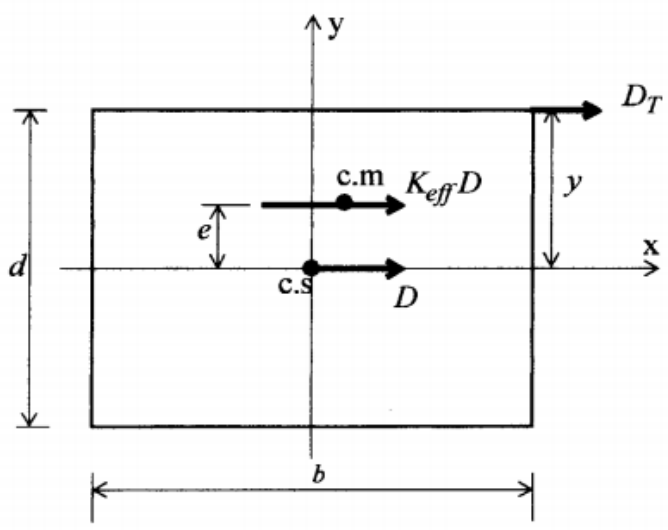

Figure 3.5 Plan dimensions for the calculation of maximum total displacement [4]

Chapter 4: Prototype Buildings

Two office buildings for location at Vancouver City Hall, BC, Canada were selected as the prototype buildings for this study. Figure 4.1 shows the dimensions of the prototype buildings. Building A is a 5-story building with a floor area of 45 m by 63 m and a total building height of 18.85 m. Building B is a 15-story building with a floor area of 27 m by 27 m and a total building height of 55.35 m. The site class was assumed to be in Class C according to NBCC [19]. LRBs were used at the base level as the isolation devices. As shown in Figure 4.2, the LRBs were grouped into three types, based on the locations (Type A = center, Type B = side, and Type C = corner). The superstructure was designed using perimeter steel eccentrically braced frames (EBFs) shown in Figure 4.2.

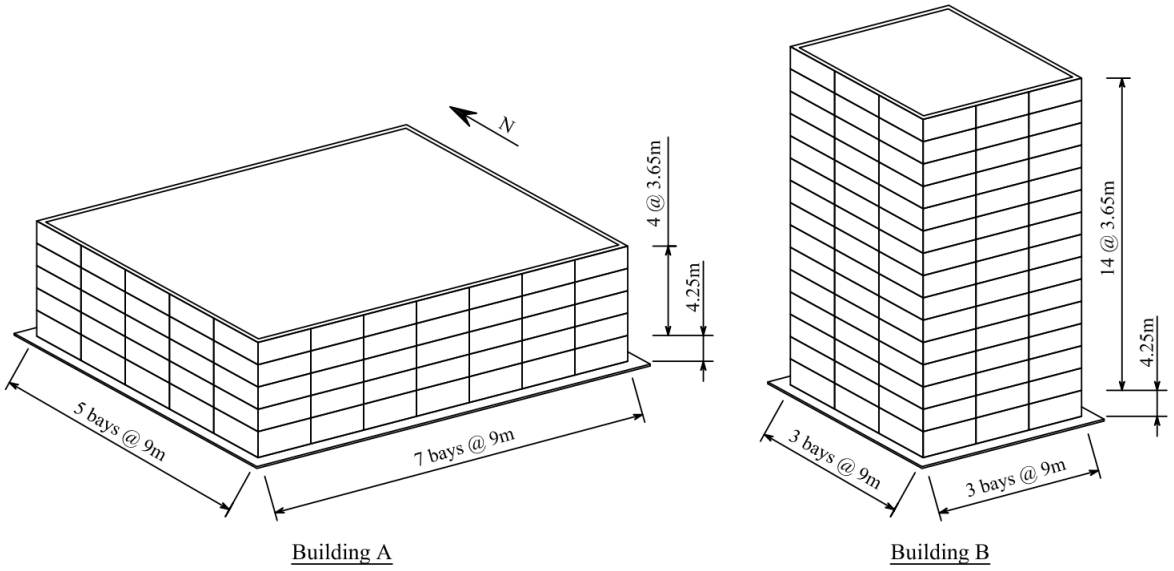

Figure 4.1 Isometric view of Buildings A and B

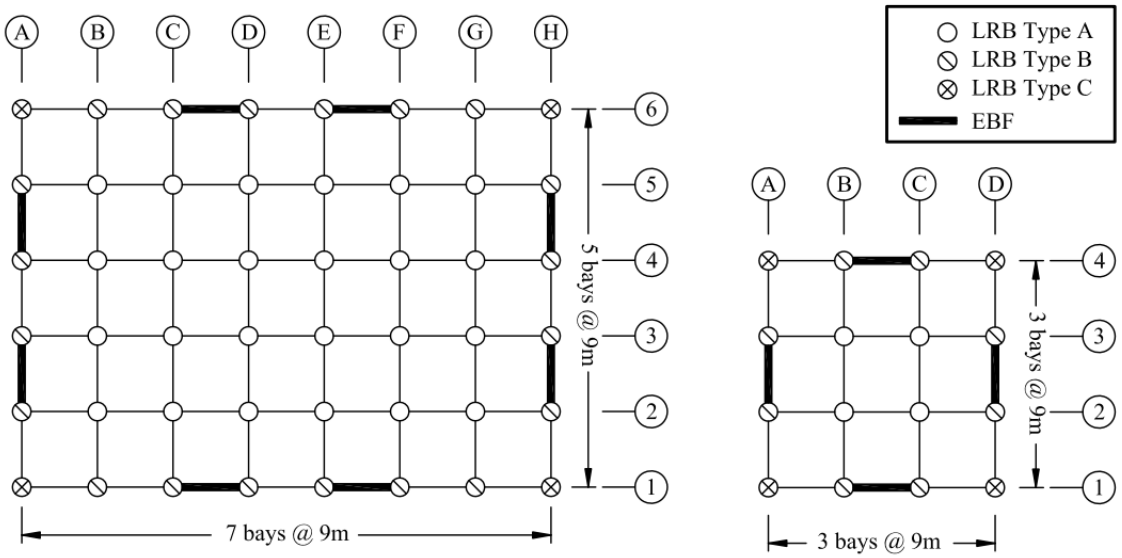

Figure 4.2 Plan layout of Buildings A and B

4.1 Bilinear Model Parameters

The values of spectral acceleration of the site-specific spectrum with a hazard level of a 2% probability of exceedance in 50 years (2/50), and a damping ratio of 5% are shown in Table 4.1. The S_a values were generated by Natural Resources Canada (NRC) in a site-specific seismicity hazard report [27] for Vancouver City Hall, with site Class C. According to NBCC [19], the design spectrum was constructed using the S_a and the corresponding S_d on T = 0.2, 0.5, 1, 2, 5, and 10 sec.

Table 4.1 Site specific spectrum for Vancouver City Hall, 2/50 [27]

T [sec]	PGA	0.05	0.1	0.2	0.3	0.5	1	2	5	10
S_a [g]	0.366	0.446	0.678	0.844	0.851	0.753	0.424	0.257	0.081	0.029

Each prototype building was designed based on three different target periods (T_p). For building A, 3, 4, and 5 times the fixed based period were selected as the target isolated periods; for building B, 1.5, 2, and 2.5 times the fixed base period were chosen. The NBCC requires that the isolation period should be larger than three times the fixed base period. However, this requirement resulted in unpractically large LRBs for Building B. The LRBs designed based on the selected target periods mentioned above had reasonable sizes.

As explained in Chapter 3, the target damping ratio should also be defined prior to the design of the bilinear model. The target damping ratio can be optimized by minimizing the base shear for the superstructure. Figure 4.3 illustrates the relationship between the damping ratio and the normalized based shear for each period. In this case, for a target period, a single target damping ratio was selected at the bottom of each curve. The selected damping ratio is listed in Table 4.2.

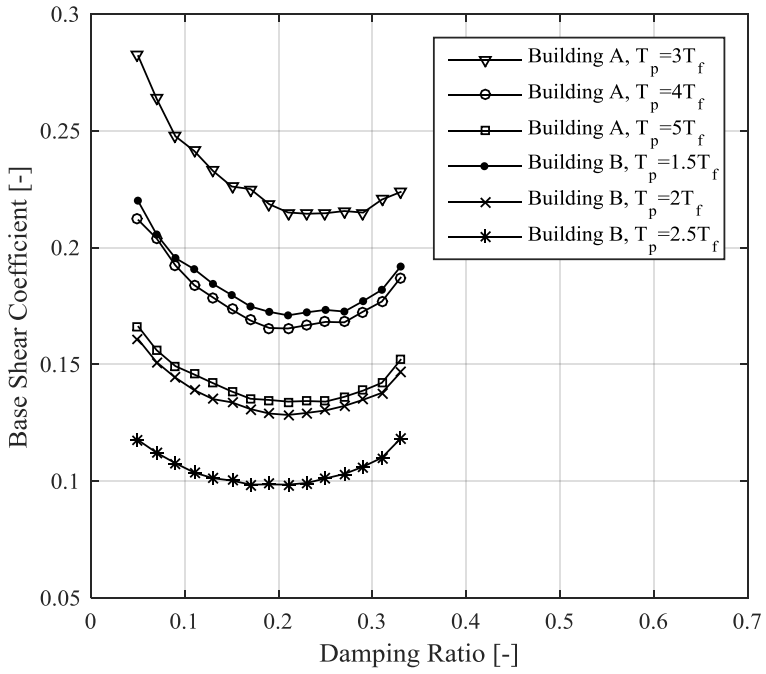

Figure 4.3 Optimization of damping ratio

Based on the target period and damping ratio, the bilinear model parameters can be calculated using the capacity spectrum method and the iterative process in Chapter 3. The design results are shown in Figure 4.4 and Table 4.2.

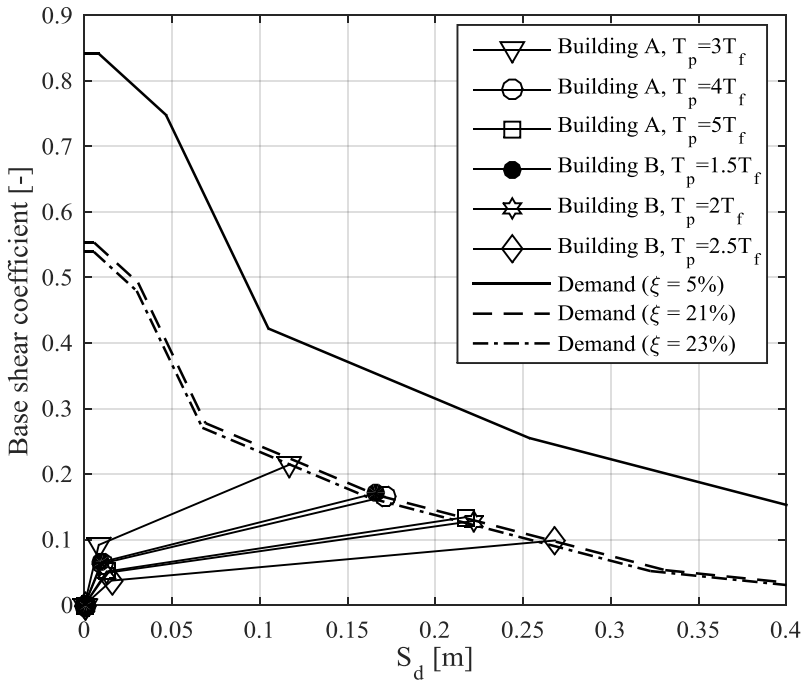

Figure 4.4 Bilinear models

Table 4.2 Bilinear model parameters

Building	T_f **[sec]**	W **[kN]**	T_p	ξ_{eff}	V_s/W	Q/W	K_2/W **[m^{-1}]**	D_{max} **[m]**	D_{Tmax} **[m]**
A	0.63	66564	$3T_f$	23%	0.215	0.083	1.127	0.117	0.140
			$4T_f$	21%	0.165	0.058	0.634	0.171	0.205
			$5T_f$	21%	0.134	0.047	0.406	0.217	0.260
B	1.63	49231	$1.5T_f$	21%	0.171	0.060	0.673	0.167	0.192
			$2T_f$	21%	0.128	0.045	0.379	0.222	0.255
			$2.5T_f$	21%	0.099	0.035	0.242	0.268	0.308

4.2 Superstructure Design

Eccentrically braced frames were selected as the seismic force resisting system (SFRS) for the superstructure of the prototype buildings. An EBF application in a real project is presented in Figure 4.5. The EBF has high elastic stiffness and high ductility at large story drift. The plastic mechanism of the EBF is controlled by a small segment on the beams called the link [28].

Figure 4.5 Eccentrically braced frame (EBF) [28]

According to NBCC [19], the superstructure of an isolated building should be designed to remain elastic during earthquakes. The eccentrically braced frames were designed using the base shear of $3T_f$ and $1.5T_f$ for buildings A and B, respectively, since they provided the maximum base shear among the three target periods for each building. The base shear was distributed vertically along the height of the superstructure as expressed by:

$$F_x = V_s \frac{h_s W_x}{\sum_{i=1}^{N} h_i W_i} \qquad 4.1$$

where W_x and W_i are the weights at levels x and i, h_x and h_i are the respective heights of the structure above the isolation level.

Regarding 10% of the eccentricity of the lateral seismic force, the base shear force transmitted to the EBFs on one side is equal to $0.6F_x$. The link shear can be obtained from the free body diagram of half of a segment of the frame as shown in Figure 4.6.

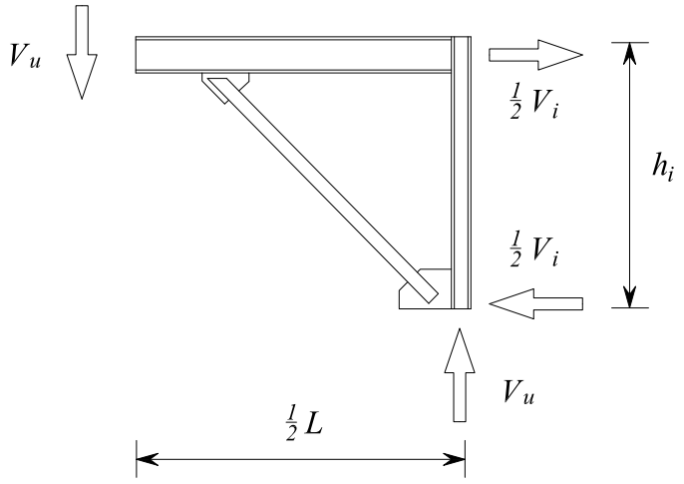

Figure 4.6 Free-body diagram showing the link shear and frame shear of EBF

The link shear can thus be calculated as:

$$V_u = \frac{V_i h_i}{L} \tag{4.2}$$

where V_i and h_i are the frame shear and story height, respectively; and L is the bay width.

Table 4.3 and Table 4.4 present the results of the link shear calculation of the EBFs.

Table 4.3 Calculation of link shear (Building A)

Level	W_x (kN)	h_x (m)	F_x (kN)	F_x per EBF (kN)	V_x (kN)	V_u (kN)
5th	7299	3.65	3861.098418	1158.329525	1158.33	469.76697
4th	11795	3.65	4057.104292	1217.131288	2375.461	963.38133
3rd	11853	3.65	3098.024923	929.407477	3304.868	1340.3077
2nd	11853	3.65	2118.995402	635.6986206	3940.567	1598.1188
1st	11882	4.25	1142.754965	342.8264894	4283.393	2022.7136
Base	11882	-	-	-	-	-

Table 4.4 Calculation of link shear (Building B)

Level	W_x (kN)	h_x (m)	F_x (kN)	F_x per EBF (kN)	V_x (kN)	V_u (kN)
15th	1923.0183	55.35	599.182495	404.4481841	404.4482	164.02621
14th	3082.1283	51.7	897.0142231	605.4846006	1009.933	409.58385
13th	3082.1283	48.05	833.685366	562.737622	1572.67	637.80522
12th	3082.1283	44.4	770.3565088	519.9906435	2092.661	848.69031
11th	3082.1283	40.75	707.0276517	477.2436649	2569.905	1042.2391
10th	3139.9326	37.1	655.7711573	442.6455312	3012.55	1221.7565
9th	3139.9326	33.45	591.2545879	399.0968468	3411.647	1383.6124
8th	3139.9326	29.8	526.7380185	355.5481625	3767.195	1527.807
7th	3139.9326	26.15	462.2214491	311.9994782	4079.195	1654.3401
6th	3139.9326	22.5	397.7048797	268.4507938	4347.646	1763.2118
5th	3203.4602	18.85	339.929419	229.4523578	4577.098	1856.2675
4th	3203.4602	15.2	274.1075421	185.0225909	4762.12	1931.3044
3rd	3203.4602	11.55	208.2856652	140.592824	4902.713	1988.3226
2nd	3203.4602	7.9	142.4637883	96.16305713	4998.876	2027.3221
1st	3232.9072	4.25	77.34642386	52.2088361	5051.085	2385.2347
Base	3232.9072	-	-	-	-	-

The links were designed according to the clauses in CSA S16-14 [29]. Once the link sections were obtained, the beams, columns, and braces were capacity designed based on the link resistance. Table 4.5 shows the structural member sections of the superstructure for buildings A and B.

Table 4.5 Structural member sections

Building	Level	EBF				Gravity Column
		Link	Beam	Column	Brace	
A	4 - 5	W410x67	W610x113	W250x58	W310x107	W250x67
	2 - 3	W530x165	W690x192	W310x143	W360x162	W250x101
	1	W610x241	W760x257	W310x226	W360x196	W250x101
B	11 - 15	W610x113	W690x192	W360x262	W310x202	W250x101
	6 - 10	W690x240	W690x289	W360x677	W310x313	W310x202
	1 - 5	W760x314	W840x359	W360x1068	W360x347	W310x313

4.3 LRB Properties

Based on the bilinear model parameters calculated in section 4.1, the characteristic strength and post-elastic stiffness of the isolation systems were distributed to each isolator based on the tributary area. In this case, the bilinear model of each single LRB was obtained. Table 4.6 lists the LRB properties used in this study. The rubber shear modulus was applied based on different LRB locations.

Table 4.6 LRB properties

Property	Notation [unit]	Value
Rubber shear modulus	G_r [MPa]	1.1 (Type A), 0.6 (Type B), 0.3 (Type C)
Rubber bulk modulus	K [MPa]	2000
Lead yield strength	F_{yl} [MPa]	10
Single shim thickness	t_s [mm]	2
Single rubber layer thickness	t_r [mm]	3, 9, 15

The design axial force (P_D) of the LRB was calculated based on a load combination in NBCC [19]:

$$P_D = 1.0D + 1.0E + 0.5L + 0.25S \quad (4.3)$$

where D, L, and S are dead, live, and snow loads, respectively; E was considered as the axial load on LRB caused by overturning from the static equivalent earthquake load. Table 4.7 lists the design axial force for the LRBs in the prototype buildings.

Table 4.7 LRB Design axial force

	Building A			Building B		
T_p	$3T_f$	$4T_f$	$5T_f$	$1.5T_f$	$2T_f$	$2.5T_f$
Type A	2787	2672	2598	9285	8708	8304
Type B	1691	1565	1485	7538	6527	5820
Type C	957	869	812	5217	4351	3745

(unit: kN)

As presented in the previous chapter, different combinations of LRB geometric parameters result in the same bilinear curve. In this study, the single rubber thickness (t_r) was selected as 3, 9, and

15 mm to represent the typical range of rubber thickness used in the industry. With each of the selected single rubber thicknesses (example t_r = 3 mm), different number of n_r would result in different axial capacity. In this study, the number of n_r was increased (hence the buckling capacity of the LRB would increase accordingly) to identify the axial capacity (P_{cr}) needed to resist the factored design load shown in Table 4.7, when the shear deformation reached the maximum total displacement. In this study, n_r was selected to achieve different levels of capacity, which can be generalized as an amplification factor defined as:

$$Amplification\ factor\ = \frac{P_{cr}}{P_D} \tag{4.4}$$

4.4 Numerical Modeling Approach

The prototype buildings were modeled in 3D in OpenSees Navigator [30] as shown in Figure 4.7. The LRBs were modeled using the advanced numerical element called "*LeadRubberX*" [22, 24] which has 2 nodes and 12 degrees of freedom. This element requires only the geometric and material properties of an LRB. Figure 4.8 shows the hysteresis of a *LeadRubberX* element under different axial loads. The result shows that the behavior of the LRB changes significantly with the presence of different axial loads. The superstructures were designed to remain elastic according to NBCC [19]. Hence these elements were modeled using elastic elements. The peak forces in these elements were checked to ensure that the forces do not exceed the elastic limit. The floor above the isolator was modeled using a rigid elastic slab [31]. Rigid diaphragm constraints were used to model the floors on the superstructures.

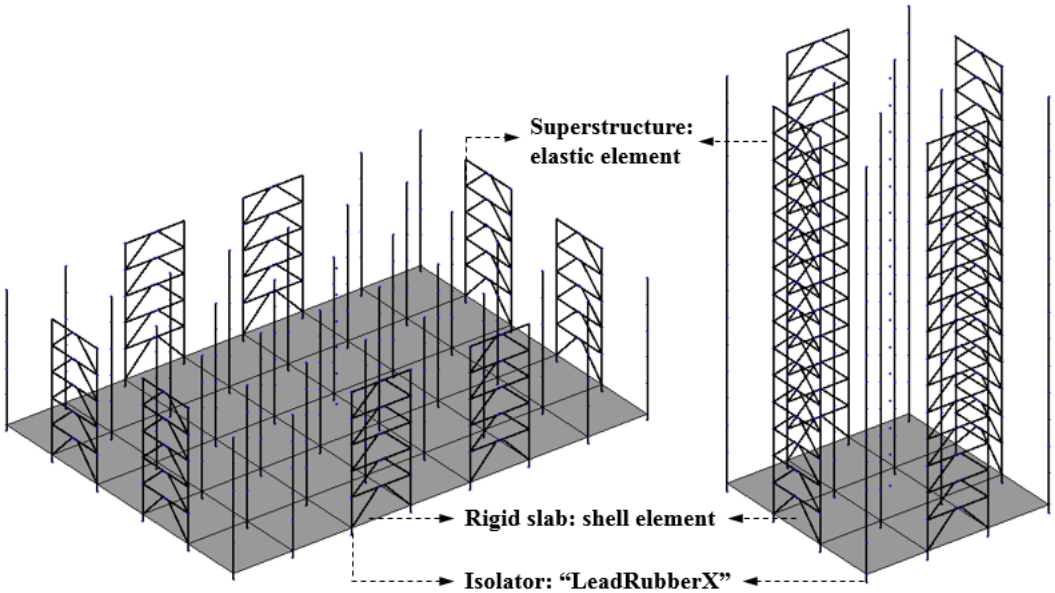

Figure 4.7 OpenSees Navigator models

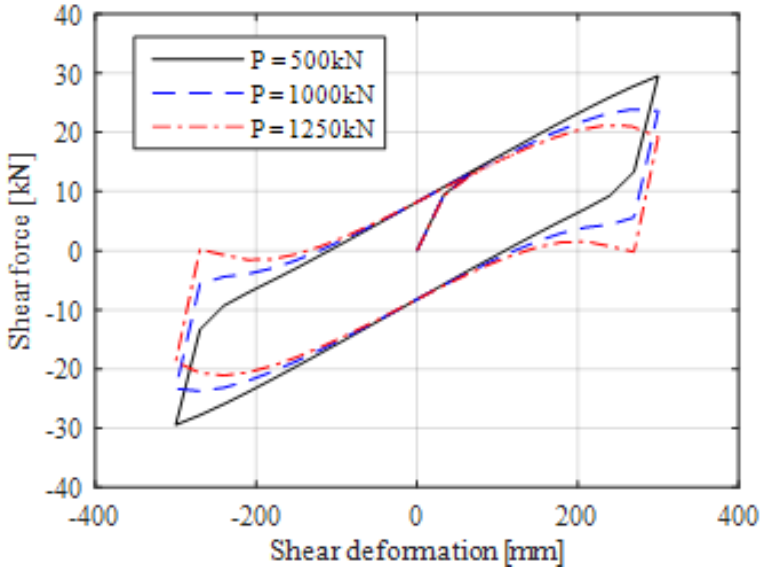

Figure 4.8 Effect of axial load (*P*) on shear behavior using *LeadRubberX*

Mass was assigned as lumped masses on the master nodes at each floor, where the masses in two horizontal directions and a torsional mass at each floor were included. The master nodes at each floor were shifted at 5% of the building plan dimensions to take accidental eccentricity into account. Gravity loads were applied to columns using the load combination shown in Equation 4.3. 2.5% stiffness-proportional damping was assigned to the first isolation mode (T_p) shown in Table 4.8.

Table 4.8 Building periods

Building	T_f **[sec]**	**Model**	T_p **[sec]**
A	0.63	Building A - 3.0T_f	2.1
		Building A - 4.0T_f	2.8
		Building A - 5.0T_f	3.4
B	1.63	Building B - 1.5T_f	2.9
		Building B – 2.0T_f	3.7
		Building B - 2.5T_f	4.5

Chapter 5: Seismic Hazard Analysis

This chapter summarizes the source and mechanism of the earthquakes contributing to the seismic hazard risk in Southwestern British Columbia; the procedure for ground motion selection for the time history analyses of the prototype buildings will be demonstrated. The ground motion selection procedure was based on the NBCC 2015 Structural Commentary using the target spectrum, and the deaggregation results provided by Natural Resource Canada (NRC).

5.1 Seismicity in Southwestern British Columbia

The prototype building is located in Southwestern British Columbia, a part of the Ring of Fire area where a tremendous number of earthquakes occur each year. Vancouver is in Canada's region of highest seismic hazard, as seen in Figure 5.1. This region is near the Cascadia subduction zone, stretching from Southern British Columbia to Northern California, where several tectonic plates are in collision, as shown in Figure 5.2. The Juan de Fuca Plate, the Explorer Plate, and the Gorda Plate are subducting beneath the North American Plate at a rate of 2-4 cm/yr [32], and this process produces three types of earthquake: crustal, subcrustal, and subduction. Figure 5.3 illustrates the sources of Cascadian earthquakes.

Crustal Earthquakes occur within the North American Plate and are caused by a collision between blocks of the continental crust [33]. This type of earthquake generally occur at depths of less than 35 km [34]. Although crustal earthquakes are commonly seen in this region, very few of them are

large enough to cause damage. Two large crustal earthquakes have taken place during British Columbia's history, M7.3 in 1946 and M7.0 in 1918; both occurred on Vancouver Island [34].

Subcrustal earthquakes take place within the oceanic plates as they descend beneath the North American Plate, as shown in Figure 5.3. This type of earthquake generally has a depth of below 30 km and a magnitude less than M7.5 [35]. Two main sources of subcrustal events are located along the west coast of Vancouver Island and beneath Puget Sound [36]. The most severe subcrustal earthquakes in this region are concentrated in the Puget Sound area. Examples include the 2001 M6.8 in Nisqually, the 1965 M6.5 in Seattle, and the 1949 M6.8 in Olympia [35].

The last type of earthquake, the subduction earthquake, occurs when the interface between the oceanic and North American plate rupture due to accumulated energy in the "locked" zone [36]. This type of earthquake is the rarest and most damaging. They can be as large as M9 and lead to severe aftershocks and destructive tsunamis [35]. Geological evidence shows that an M9 subduction earthquake occurred in 1700 at the southwestern coast of Vancouver Island; this was the most recent subduction earthquake to take place in the Cascadian subduction zone [37].

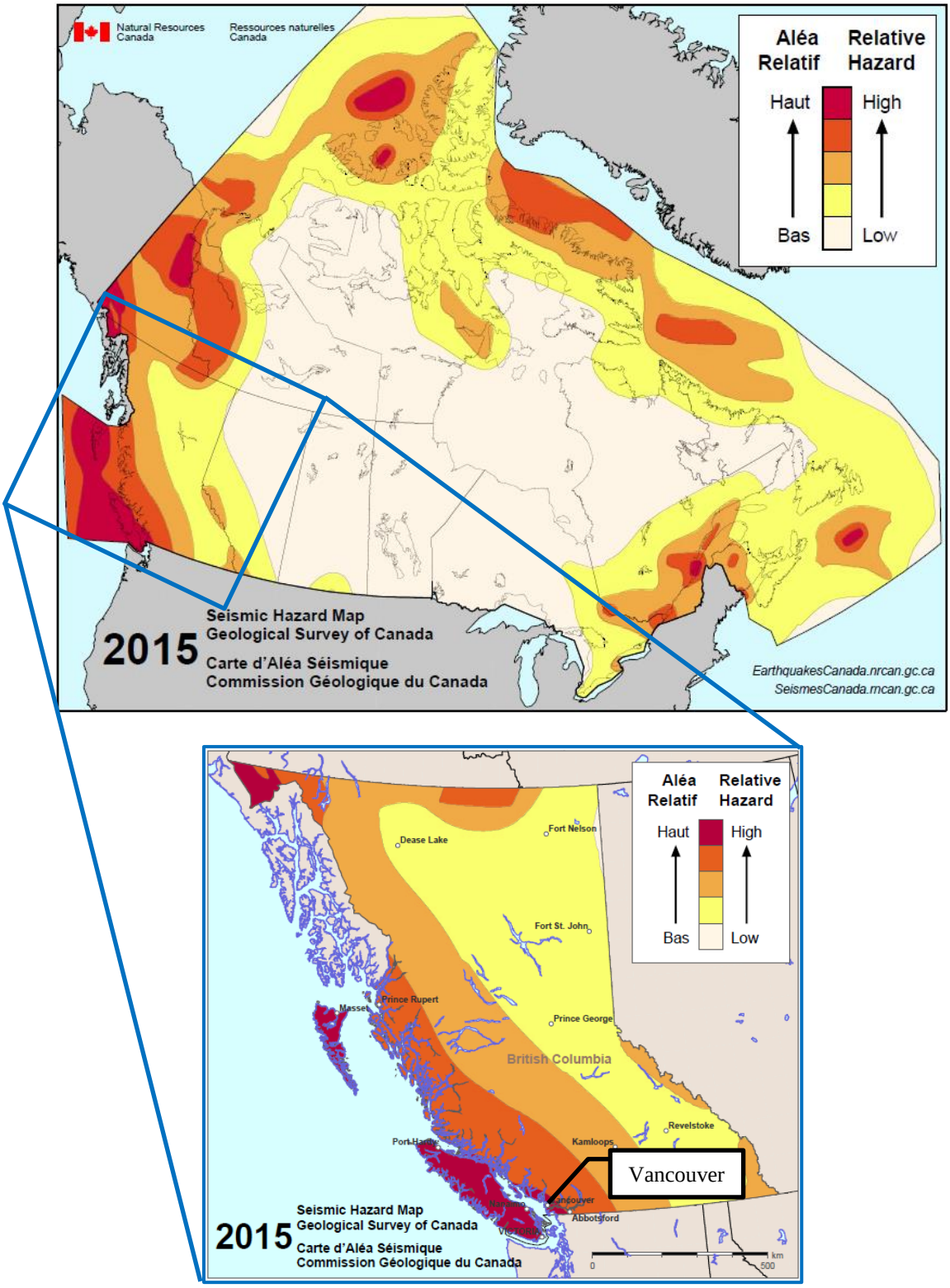

Figure 5.1 Simplified Seismic Hazard Map for Small (1-2 Story) Structures [38]

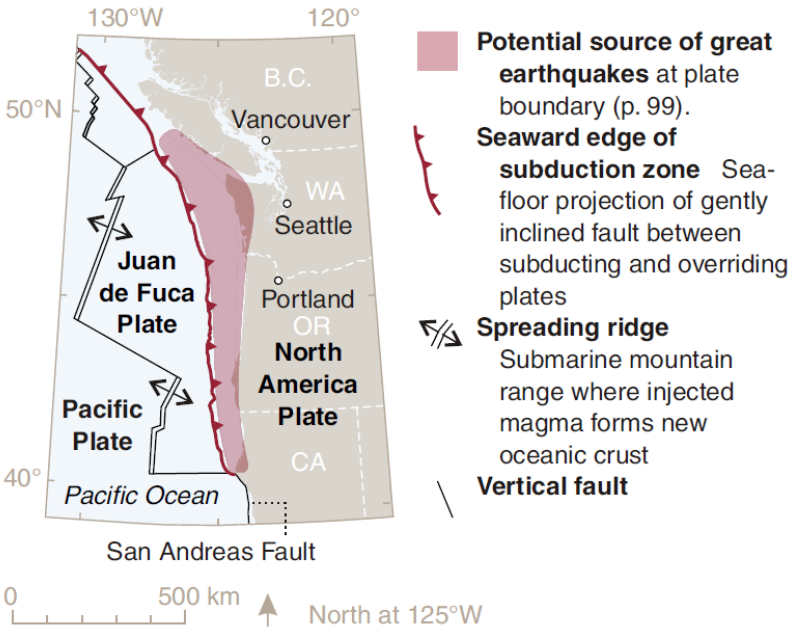

Figure 5.2 The Cascadian subduction zone [39]

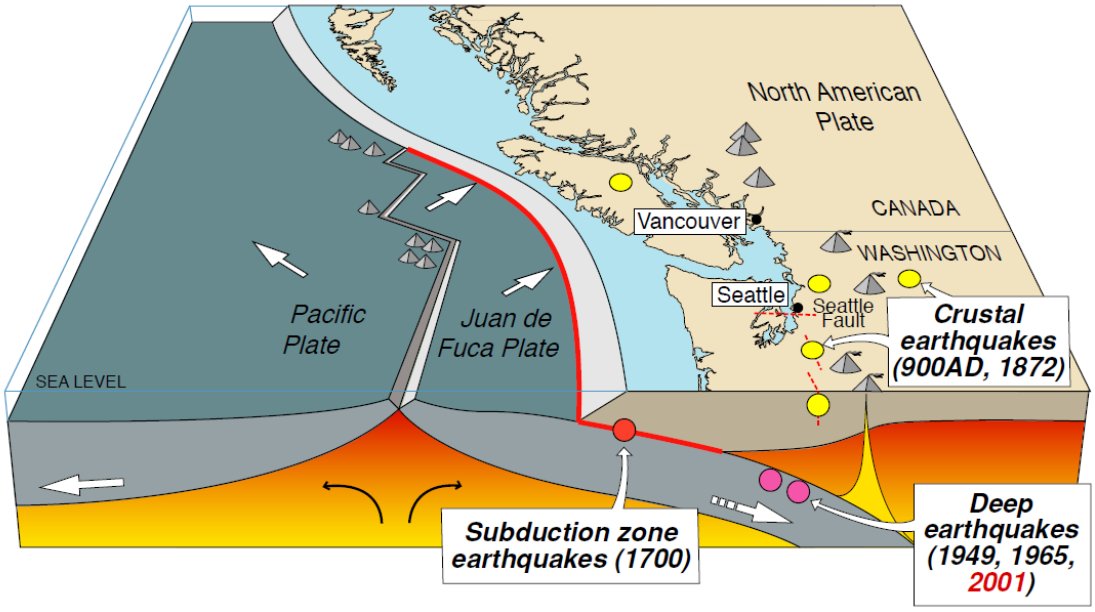

Figure 5.3 Cascadian earthquake source [40]

5.2 Probabilistic Seismic Hazard Analysis

Probabilistic seismic hazard analysis (PSHA) is a procedure used to quantify the uncertainties of ground shaking in order to assess the future seismic risk of a site. The system entails the following steps: 1) Identifying all seismic sources that could cause damage to the site; 2) Identifying the distribution of the rate of the earthquakes with magnitudes exceeding every considered level; 3) Identifying the distribution of the distance from the earthquakes to the site; 4) Predicting the distribution of the ground motion intensity as a function of magnitude, distance, and other factors.; 5) Combining all the information above and calculating the rate of exceedance for different ground motion intensities [41].

One of the main results generated from PSHA is the uniform hazard spectrum for the site. PSHA provides the relationship between the rate of exceedance and the spectral acceleration for each period, following which the data for certain rate levels can be plotted versus the corresponding period. The process is illustrated in Figure 5.4.

Hazard deaggregation is another crucial result of PSHA. Deaggregation can be calculated by dividing the total hazard range into different magnitudes and distances for earthquakes under consideration for the site. These results help to provide a better understanding of the predominant seismic source for buildings with different periods, leading to a better selection of ground motions for time history analyses [42]. Particularly for the Vancouver area where the seismic source is complicated, as specified in the previous subsection, it is crucial to select ground motions from diverse sources for their dominated period range based the deaggregation results.

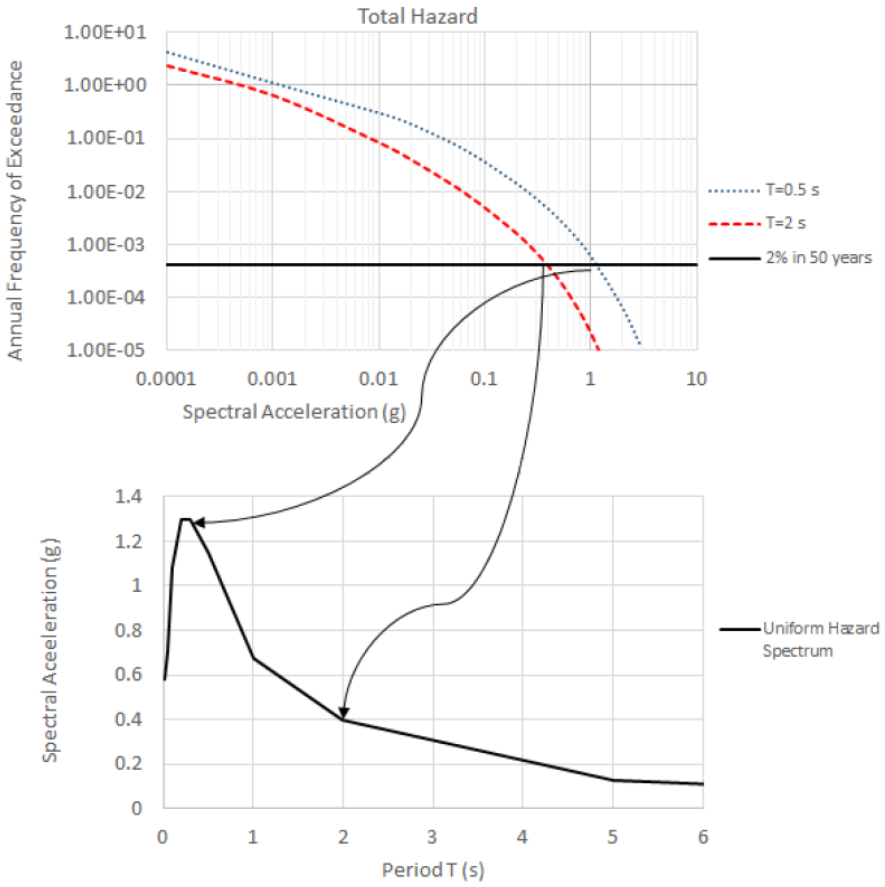

Figure 5.4 Generating the design spectrum from the PSHA results [43]

5.3 Seismic Hazard Model for NBCC 2015

In NBCC 2015, the seismic design values are provided in terms of 5% damped spectral acceleration at a hazard level of 2% probability of exceedance in 50 years (2% in 50 years). The design values are developed based on Canada's 5th Generation seismic hazard model [44].

In western Canada, several seismic sources have been updated for the 5th Generation model, including three fault sources (the Juan de Fuca, Explorer and Winona segments) in the Cascadia subduction zone, an updated treatment of the Queen Charlotte Island faults, and five added faults

in the Yukon and Alaska region [45]. In addition to the seismic source, ground motion prediction equations (GMPEs) are also a key component of the new seismic hazard model. GMPEs predict the spectral acceleration of ground motions as functions of magnitude and distance. The database for the ground motion records has grown rapidly, leading to an improvement in the GMPEs. In order to provide a simple, efficient, and flexible solution for considering the epistemic uncertainty in the GMPEs, a three-equation approach is suggested for the new seismic hazard model. This approach uses three representative GMPEs (i.e., central, lower, and upper) rather than a weighted combination of equations [46].

5.4 Ground Motion Selection

The ground motion selection for this study was based on the procedure summarized in the Structural Commentary of NBCC 2015. The Commentary has specified two methods for determining the target response spectrum for ground motion selection. Method A uses a single target spectrum, while two or more site-specific scenario target response spectra are required for Method B. Method A was chosen for this study. The values for the spectral acceleration of the site specific spectrum with a hazard level of 2% probability of exceedance in 50 years (2/50) and a damping ratio of 5% for the site are shown in Table 5.1 and Figure 5.5. The S_a values were generated by NRC as Site Class C in a site specific seismicity hazard report [27] for Vancouver City Hall.

Table 5.1 The site specific spectrum for Vancouver City Hall, 2/50 [27]

T [sec]	0	0.05	0.1	0.2	0.3	0.5	1	2	5	10
S_a [g]	0.366	0.446	0.678	0.844	0.851	0.753	0.424	0.257	0.081	0.029

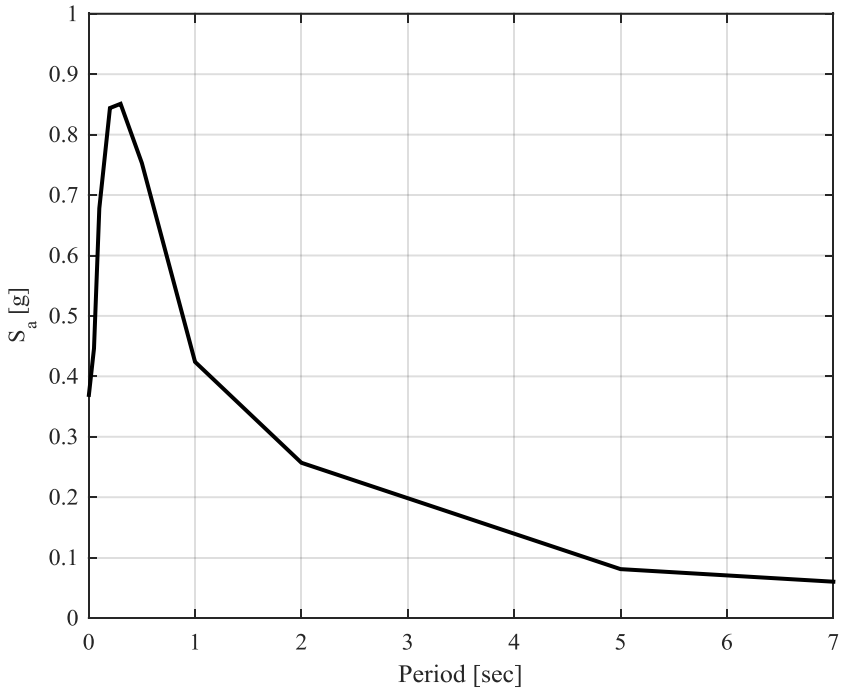

Figure 5.5 The site specific spectrum for Vancouver City Hall, 2/50

The site specific seismic hazard deaggregation of Vancouver City Hall was requested from NRC [27]. Figure 5.6 shows the seismic hazard deaggregation of 2/50 for the site at periods of 0.5, 1, 2, and 5 seconds. Based on the site specific seismic hazard analysis, the site has three dominant seismic hazard sources, namely, the crustal, subcrustal, and subduction hazard source, and the characteristic distance and magnitude ranges for earthquakes at each source are listed in Table 5.2. It can be seen from the deaggregation results that crustal and subcrustal earthquakes have a

dominant presence at low period ranges of up to 2 seconds, while subduction earthquakes make significant contribution to the hazard at long periods of greater than 1second.

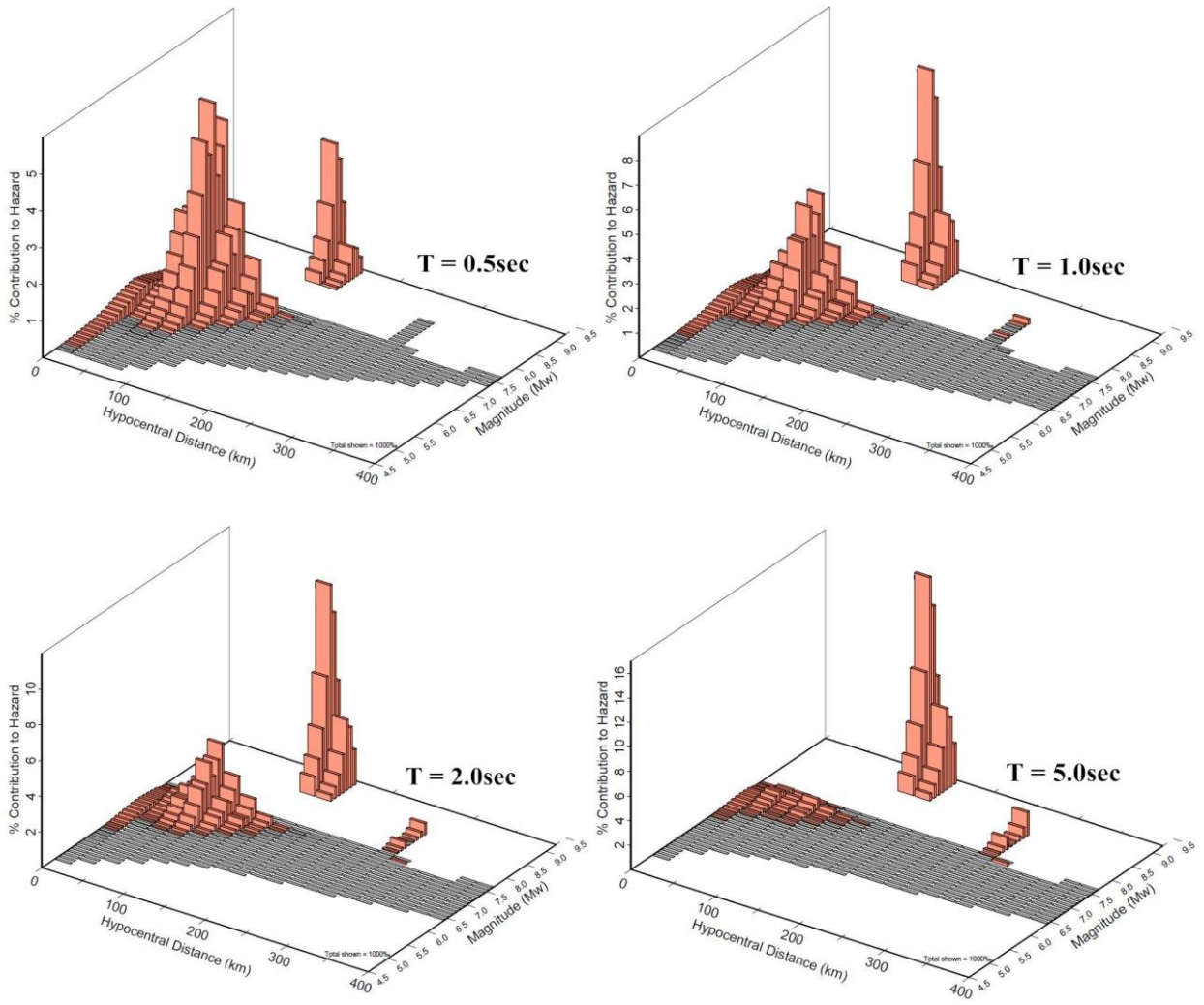

Figure 5.6 Seismic hazard deaggregation at Vancouver City Hall [27]

According to NBCC 2015, as specified in Figure 5.7, the ground motions should be scaled within a period range (T_R) of between $0.2T_1$ and $1.5T_1$ for isolated buildings where T_1 is the fundamental period of the isolated building computed using the post-elastic stiffness of the isolation system. As

specified in Chapter 4, the post-elastic periods (T_p) of the prototype buildings with different isolation systems ranges from 2.1 to 3.4sec for Building A and 2.9 to 4.5sec for Building B. For each building, in order to select ground motions for all the design periods, the total period range should cover all the individual T_R of each T_p. Therefore, the period range for Building A is defined as 0.2*2.1 - 1.5*3.4sec (0.42 – 5.1sec), and 0.2*2.9 - 1.5*4.5sec (0.58 – 6.75sec) for Building B. Scenario specific period ranges (T_{RS}) were defined for all the seismic sources that contribute to the hazard. The T_{RS} may overlap one another, and should cover the period range T_R. Table 5.2 and Figure 5.8 show the specified T_{RS} for each seismic source.

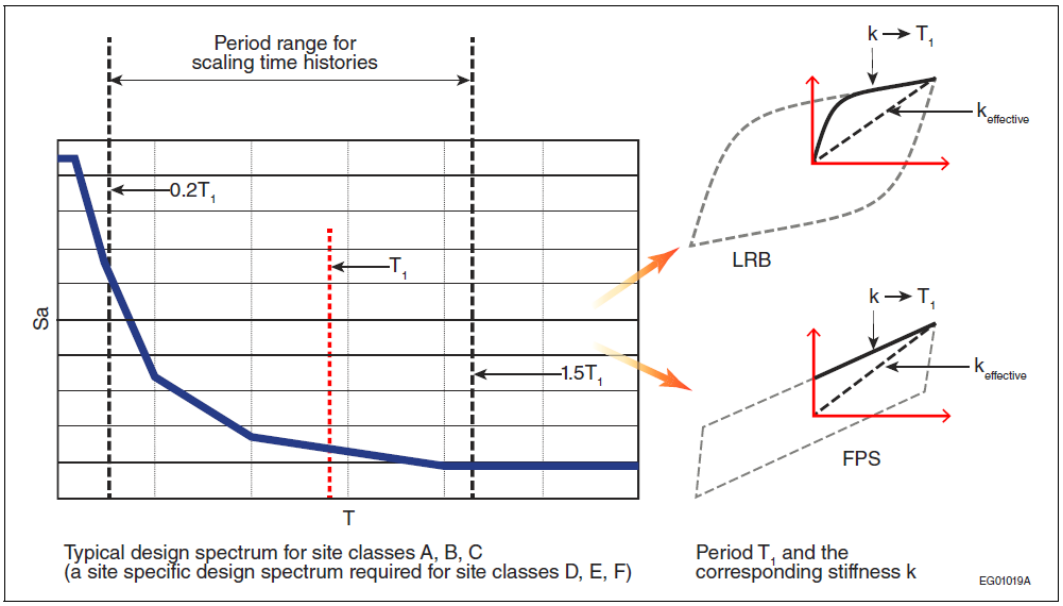

Figure 5.7 Period range of ground motion scaling for isolated buildings [19]

Table 5.2 Dominant earthquake sources for Vancouver City Hall

Source	Distance	Magnitude	T_{RS}	
			Building A	Building B
Crustal	≤ 35km	≤ M7.5	0.42 - 1.2sec	0.58 - 1.2sec
Subcrustal	35 – 140km	≤ M7.5	0.42 - 1.5sec	0.58 - 1.5sec
Subduction	120 – 300km	≥ M8.0	1 - 5.1sec	1 - 6.75sec

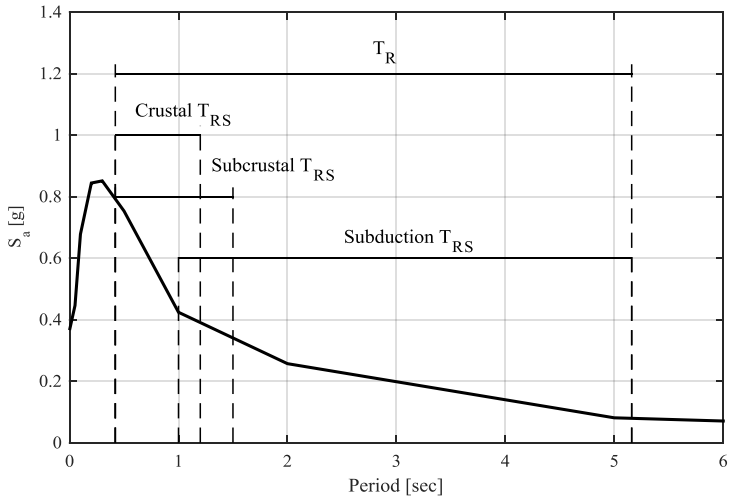

(a)

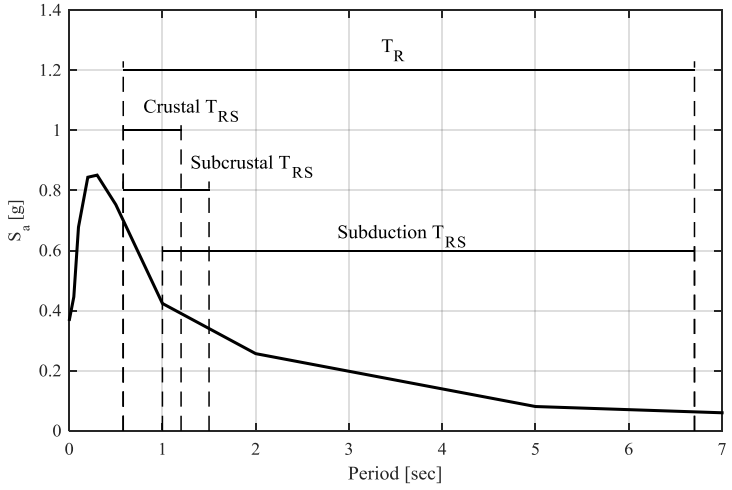

(b)

Figure 5.8 Site-specific spectrum and scenario-specific period ranges (T_{RS}) for ground motion selection (a) Building A, and (b) Building B

For each seismic source, 11 sets of ground motion records, including two horizontal components and a vertical component, were selected. Crustal records were selected from the PEER NGA-West2 database [47], while subcrustal and subduction records were selected from the S2GM database [48]. For each pair of horizontal ground motions, a geometric mean of the 5% damped response spectrum was generated and amplitude scaled to match the target spectrum within the corresponding T_{RS}. The scaled spectra of the selected ground motions are plotted in Figure 5.9 and Figure 5.10. The information on the ground motions is summarized from Table 5.3 to Table 5.5.

Table 5.3 Suite of selected crustal ground motions

Source	No.	Scale Factor		Event	M	R_{jb} (km)	R_{rup} (km)	V_{s30} (m/s)	Horizontal 1 Filename
		Building A	Building B						
Crustal	1	1.86	1.84	Northridge, CA	6.69	12.38	13.35	402.16	RSN1083_NORTHR_GLE170
Crustal	2	1.97	2.00	Imperial Valley, CA	6.53	15.19	15.19	471.53	RSN164_IMPVALL.H_H-CPE147
Crustal	3	3.41	3.32	Irpinia, Italy	6.20	22.68	22.69	574.88	RSN302_ITALY_B-VLT000
Crustal	4	1.40	1.45	Corinth, Greece	6.60	10.27	10.27	361.40	RSN313_CORINTH_COR--L
Crustal	5	3.23	3.31	Chuetsu, Japan	6.80	23.63	29.25	640.14	RSN4869_CHUETSU_65042NS
Crustal	6	2.28	2.21	Chuetsu, Japan	6.80	20.60	25.33	375.22	RSN5270_CHUETSU_NIG024NS
Crustal	7	2.22	2.12	Chalfant Valley, CA	6.19	21.55	21.92	370.94	RSN548_CHALFANT.A_A-BEN270
Crustal	8	1.64	1.79	San Fernando,CA	6.61	19.33	22.63	450.28	RSN57_SFERN_ORR021
Crustal	9	3.92	3.72	Joshua Tree, CA	6.10	21.73	22.30	396.41	RSN6875_JOSHUA_5071045
Crustal	10	1.35	1.31	Loma Prieta, CA	6.93	19.97	20.34	561.43	RSN755_LOMAP_CYC195
Crustal	11	1.49	1.54	Landers, CA	7.28	17.36	17.36	396.41	RSN881_LANDERS_MVH045

Table 5.4 Suite of selected subcrustal ground motions

Source	No.	Scale Factor		Event	M	Epicentral Distance (km)	Hypocentral Distance (km)	V_{s30} (m/s)	Horizontal 1 Filename
		Building A	Building B						
Subcrustal	12	5.99	5.78	Geiyo, Japan	6.40	79.34	94.32	379.97	Geiyo_EHM0010103241528-EW
Subcrustal	13	1.30	1.25	Geiyo, Japan	6.40	39.72	59.18	266.97	Geiyo_EHM0160103241528-EW
Subcrustal	14	6.50	6.50	Michoacan, Mexico	7.30	103.57	108.70	403.41	Mich_UNIO9701_111_S90E
Subcrustal	15	2.46	2.58	Miyagi, Japan	7.20	124.03	110.31	205.38	Miyagi_Oki_MYG0060508161146-EW
Subcrustal	16	4.48	4.21	Miyagi, Japan	7.20	244.35	247.93	548.06	Miyagi_Oki_TCG0060508161146-EW
Subcrustal	17	2.06	2.08	Nisqually, WA	6.80	53.40	70.60	327.66	Nisqually_1416a_a-125
Subcrustal	18	2.10	2.12	Nisqually, WA	6.80	45.30	66.50	347.17	Nisqually_1421a_a-200
Subcrustal	19	3.32	3.33	Nisqually, WA	6.80	28.40	60.59	312.00	Nisqually_1437a_a-270
Subcrustal	20	1.93	2.09	Olympia, WA	6.90	28.49	74.70	485.51	Olympia_OLY0A-356
Subcrustal	21	3.19	3.45	Shonshu, Japan	6.40	41.02	65.45	501.42	SHonshu_EHM0050103241528-EW
Subcrustal	22	1.42	1.53	Shonshu, Japan	6.40	33.77	61.17	560.58	SHonshu_EHM0080103241528-EW

Table 5.5 Suite of selected subduction ground motions

Source	No.	Scale Factor		Event	M	Epicentral Distance (km)	Closest Distance (km)	V_{s30} (m/s)	Horizontal 1 Filename
		Building A	Building B						
Subduction	23	4.01	3.89	Hokkaido, Japan	8.00	221.98	225.92	542.18	Hokkaido_HKD0390309260450-EW
Subduction	24	2.63	2.76	Hokkaido, Japan	8.00	224.90	164.08	648.89	Hokkaido_HKD0540309260450-EW
Subduction	25	3.10	3.20	Hokkaido, Japan	8.00	182.26	123.35	512.21	Hokkaido_HKD0930309260450-EW
Subduction	26	2.23	2.30	Hokkaido, Japan	8.00	183.55	188.29	384.05	Hokkaido_HKD1040309260450-EW
Subduction	27	4.53	4.34	Hokkaido, Japan	8.00	80.95	91.20	460.82	Hokkaido_HKD1110309260450-EW
Subduction	28	3.62	3.53	Hokkaido, Japan	8.00	264.34	267.66	455.12	Hokkaido_HKD1180309260450-EW
Subduction	29	3.15	3.09	Hokkaido, Japan	8.00	221.56	160.86	602.51	Hokkaido_HKD1270309260450-EW
Subduction	30	2.93	2.86	Tohoku, Japan	9.00	409.95	212.96	378.84	Tohoku_CHB0221103111446-EW
Subduction	31	3.61	3.43	Tohoku, Japan	9.00	383.05	186.25	409.63	Tohoku_GNM0081103111446-EW
Subduction	32	3.21	3.19	Tohoku, Japan	9.00	427.81	230.71	618.97	Tohoku_KNG0051103111446-EW
Subduction	33	3.00	2.93	Tohoku, Japan	9.00	400.65	203.72	411.33	Tohoku_TKY0061103111446-EW

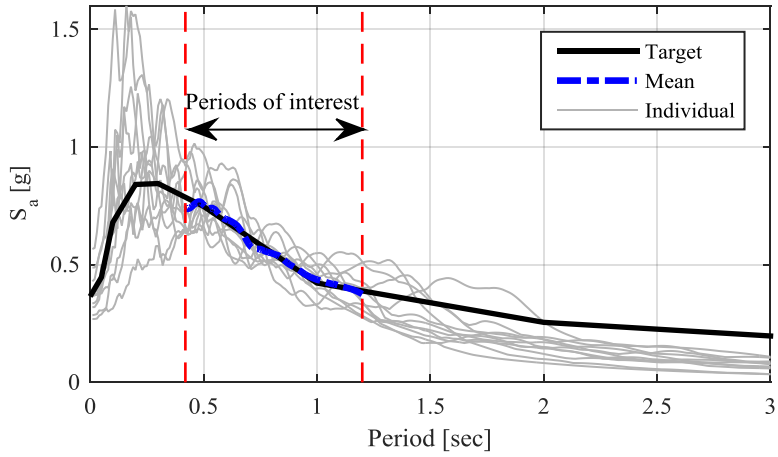

(a)

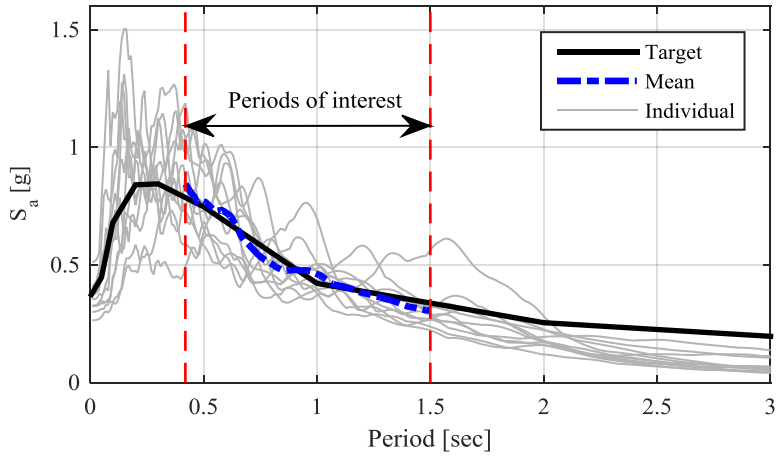

(b)

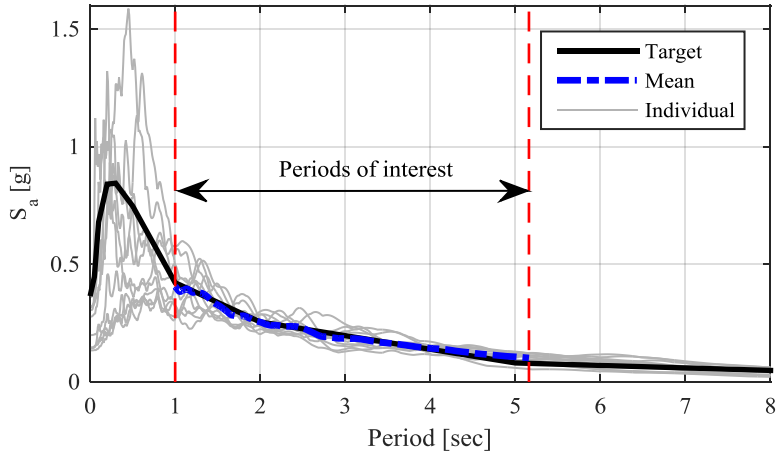

(c)

Figure 5.9 Ground motion selection for Building A (a) crustal; (b) subcrustal; (c) subduction

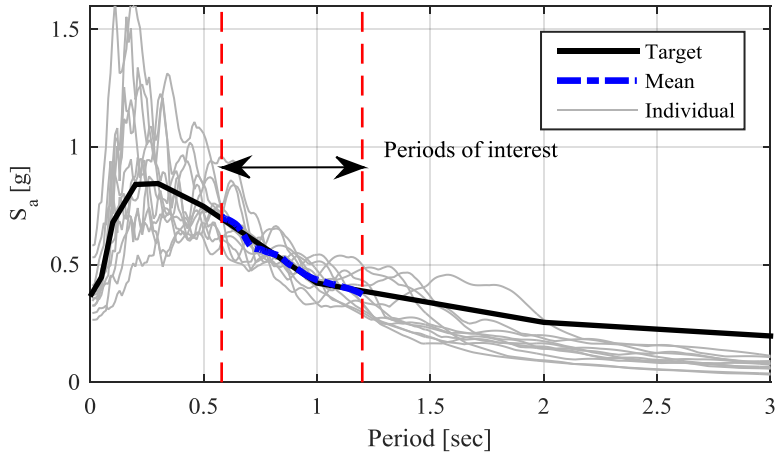

(a)

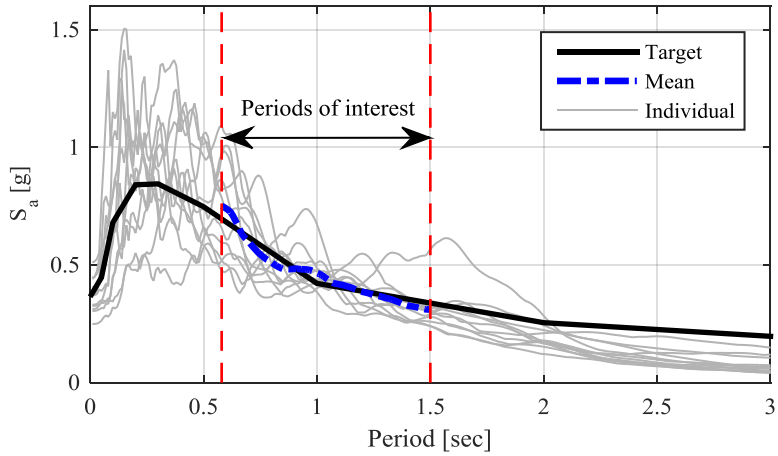

(b)

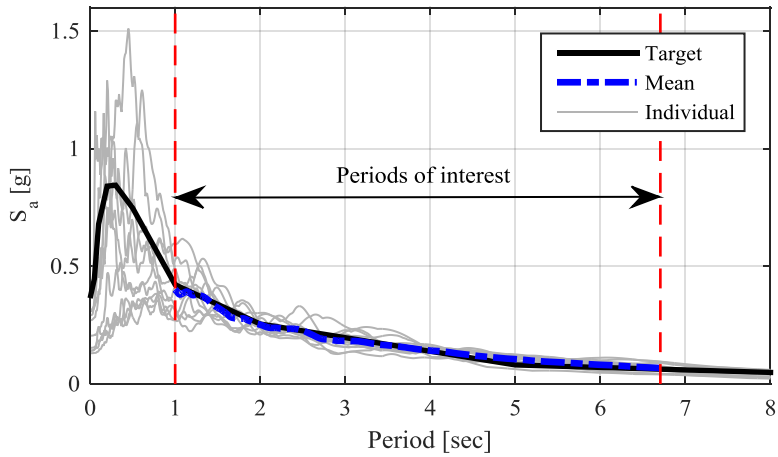

(c)

Figure 5.10 Ground motion selection for Building B (a) crustal; (b) subcrustal; (c) subduction

Chapter 6: Results of Nonlinear Time History Analysis

6.1 Structural Response without Accounting for the Buckling Failure of LRB

The nonlinear time history analyses were conducted based on the selected ground motions. The axial demands of LRBs from the analysis, where the buckling effect was not considered, were gathered. The results were calculated in the form of mean plus standard deviation of the peak response for all ground motions. Table 6.1 shows the average demand (mean plus standard deviation) for all isolators obtained from the nonlinear time history analyses over the design axial force presented in Table 4.7. The results show that the demand from dynamic analysis is close to the design axial load calculated using the CSM. This indicates that the static procedure as presented in Session 2.1 can be used to efficiently estimate the axial demand as compared with the nonlinear time history analysis when bilinear model is used. However, when the buckling behavior of LRB is explicitly modeled, as indicated in the next sub-session, the LRB designed using bilinear model (without accounting the buckling behavior) has high probability of failure. This could result to difficult structural repair and hefty repair costs.

Table 6.1 Ratio of axial load demand from CSM and time history analyses

Building A			**Building B**		
$T_p = 3T_f$	$T_p = 4T_f$	$T_p = 5T_f$	$T_p = 1.5T_f$	$T_p = 2T_f$	$T_p = 2.5T_f$
1.04	0.99	0.97	1.09	0.97	0.93

6.2 Structural Response Accounting for the Buckling Failure of LRB

During the nonlinear time history analyses, the instant critical buckling load capacity of the LRBs were calculated and compared with the real time axial demands in the LRBs. If the compressive force of any LRB exceeded the critical buckling load, LRB failure is recognized. Figure 6.1 illustrates the time series when the capacity (buckling load) and the demand (axial force) crossed, and the failed LRB recorded in the shear and axial hysteresis. The result clearly shows that the buckling load of the LRB decreased with the increase of lateral displacement.

Failure of the isolated building is defined when the first isolator failed. The probability of failure is defined as the ratio of the number of failure events over the 33 ground motions included in this study. **Error! Reference source not found.** show the probability of failure of the base isolated buildings, when the axial capacity is calculated using the amplification factor times the design loads presented in Table 4.7 (which can be calculated using CSM shown in Chapter 3 or directly from time history analysis, when the LRB is modeled using bilinear model). The result shows if the capacity of the isolator, at the maximum total displacement, is calculated using bilinear model, the base isolated building could have high probability of collapse (35% to 55% probability of collapse for Building A, and 30% to 35% probability of collapse for Building B). Besides, as the isolation period increases, the probability of collapse generally reduces. In this study, 10% was assumed as the acceptable collapse probability for practical design. In this case, the result shows an amplification factor of 2.5 is needed to ensure that both prototype buildings have acceptable probability of collapse. One interesting finding is that to achieve the same performance objective, under the same amplification factor, the LRBs designed with thinner single rubber layer thickness had higher probability of collapse.

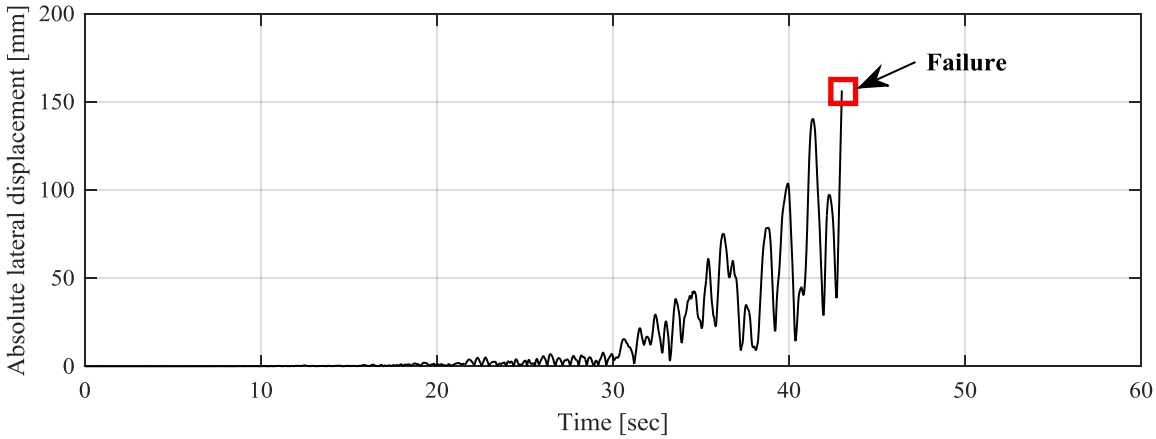

(a)

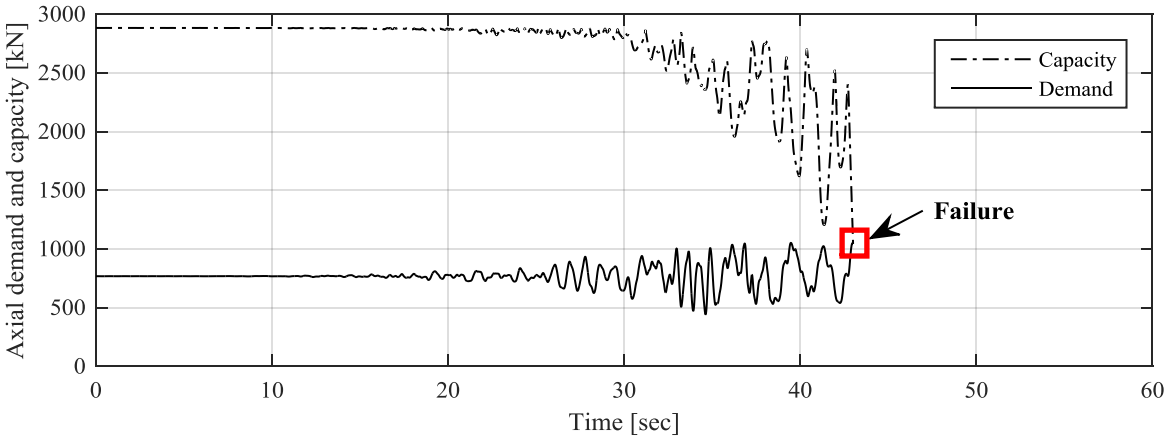

(b)

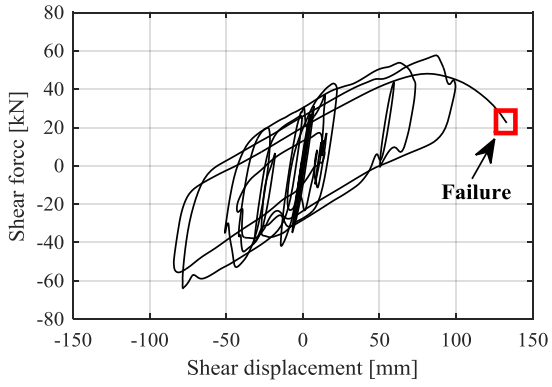

(c)

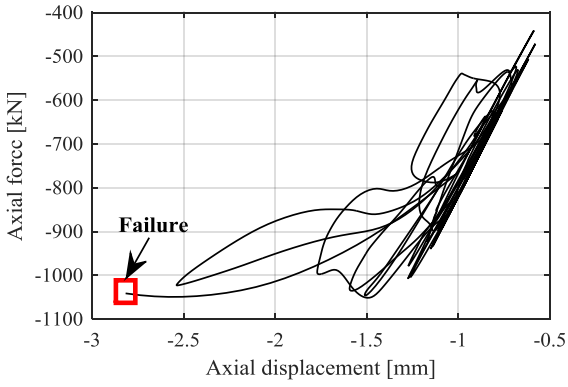

(d)

Figure 6.1 Illustration of LRB failure recognition (a) time series of absolute shear displacement; (b) time series of axial load and buckling load; (c) shear hysteresis; (d) axial hysteresis

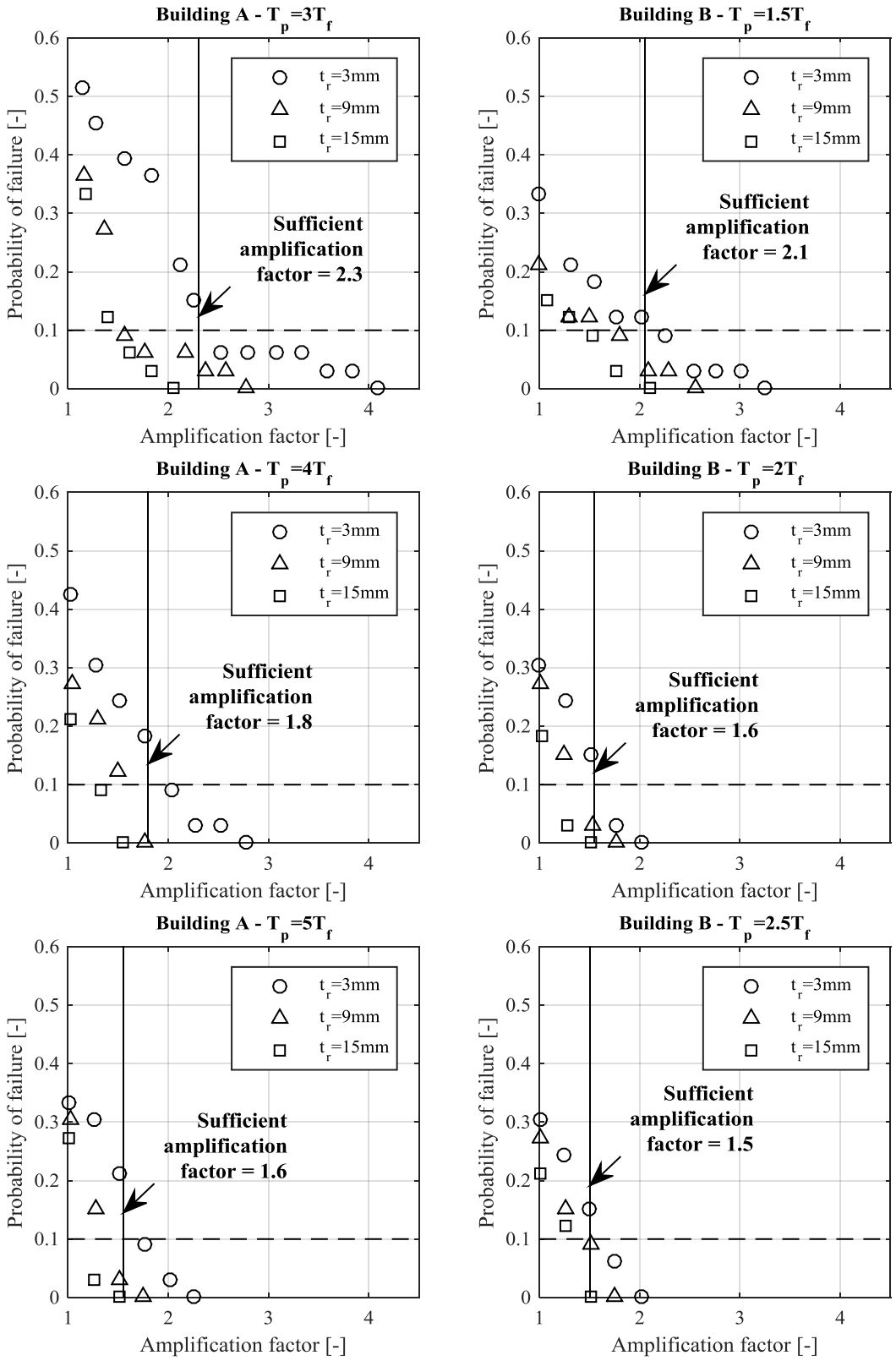

Figure 6.2 Amplification factor vs probability of failure for each period

Figure 6.3 shows the percentage of the failure from each of the seismic hazard source. The result shows that, for the short building (Building A), all the three hazard sources make significant impact for the probability of collapse. As the isolation period increases, the influence of the crustal and subcrustal earthquake decreases. As for the tall buildings (Building B), only the subduction source earthquake makes a significant impact.

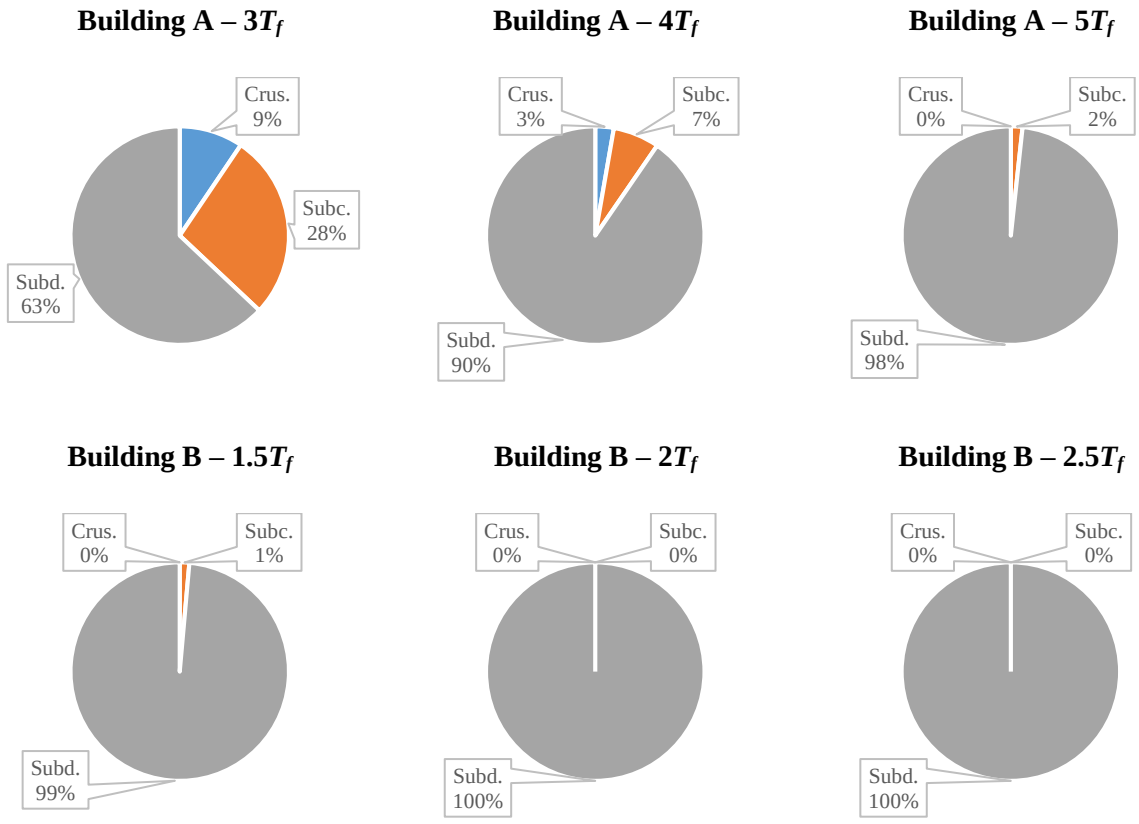

Figure 6.3 Failure distribution of crustal, subcrustal, and subduction earthquakes

6.3 Response of Safe Model

As the increasing of the amplification factor applied in the design of LRB, the probability of failure reduces accordingly. When there is no failure recognized in the model, it refers to a “safe model”.

The dynamic response of the superstructures is presented to demonstrate the effectiveness of the design procedure.

The inter-story drift ratio of the superstructure for Building A and B is plotted in Figure 6.4 and Figure 6.5, respectively. The EBF link shear is shown in Figure 6.6. For the models with the same period, the results of models with different single rubber layer thickness are extremely close to each other, hence only the results for t_r = 3mm are presented. Both the inter-story drift and the link shear were calculated using the mean plus standard deviation of the peak responses. The building with longer period has smaller response because the base shear decreases with the increasing of isolation period. The EBF links are found to remain elastic for both Building A and Building B, thus satisfy the requirement of NBCC [19].

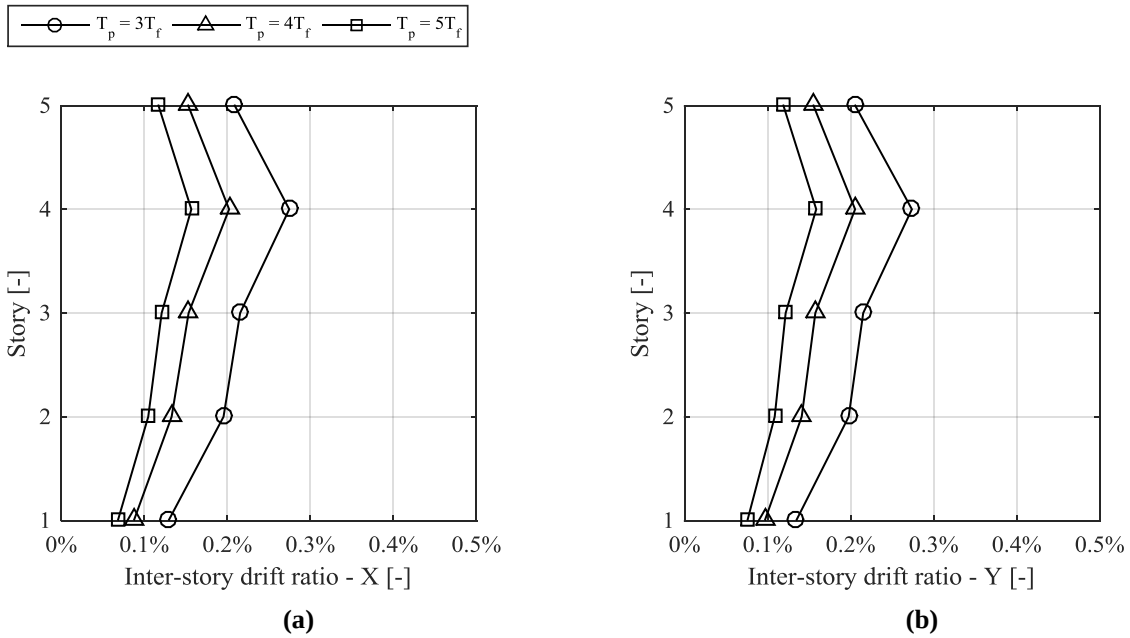

Figure 6.4 Inter-story drift ratio of Building A (a) X direction; (b) Y direction

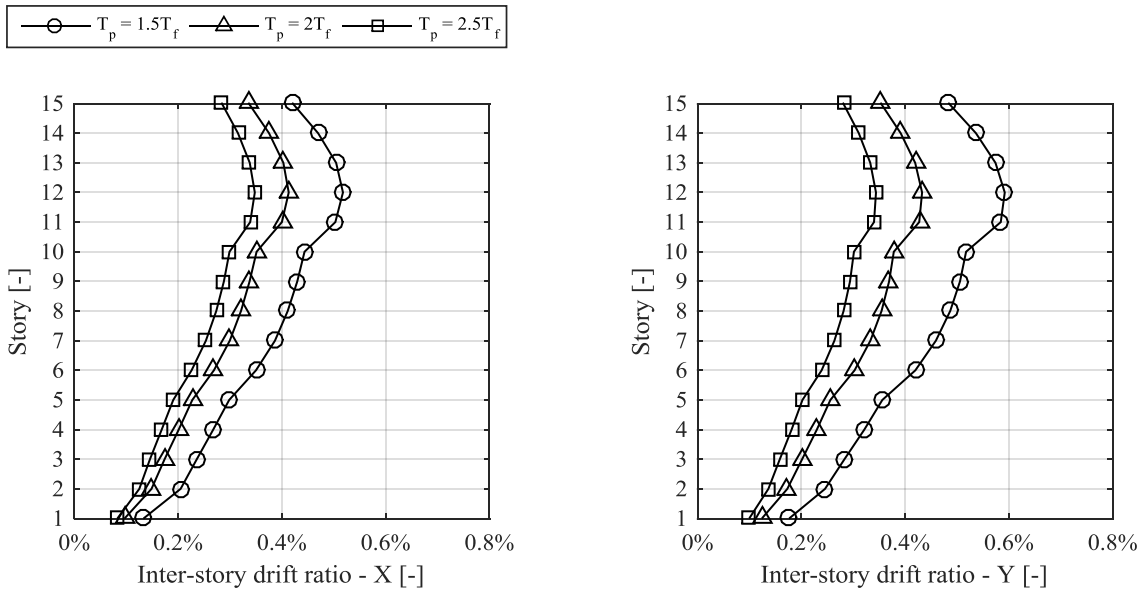

Figure 6.5 Inter-story drift ratio of Building B (a) X direction; (b) Y direction

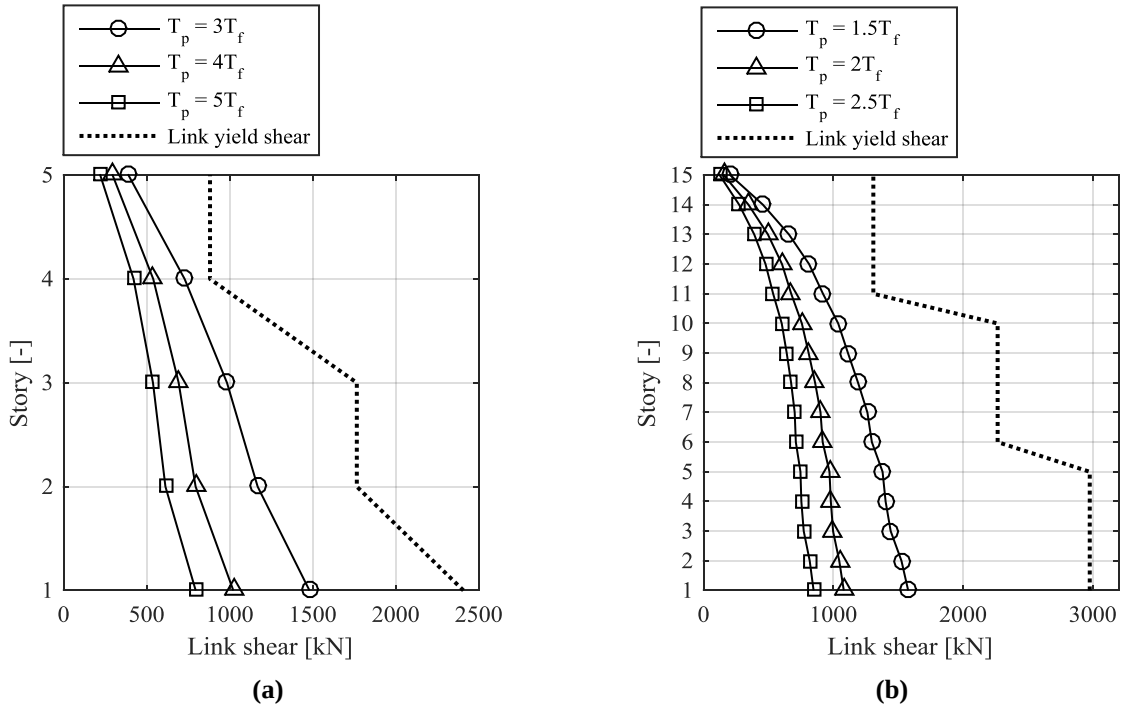

Figure 6.6 Link shear (a) Building A; (b) Building B

Chapter 7: Summaries and Conclusions

7.1 Conclusions

LRB, as a commonly-used seismic isolation system, has been implemented worldwide. As shown by previous research, LRB is vulnerable to buckling when subjected to combined large axial and shear loads. Although detailed buckling behavior of the LRB has been well investigated, the seismic performance of the base isolated building with LRB has not been systematically studied. In this study, the probability of failure for two prototype buildings, each with different LRB geometric properties and axial loads, was systematically examined. State-of-the-art LRB buckling model implemented in OpenSees was used to check the probability of failure of the prototype buildings under a range of earthquake shaking intensities. Based on the detailed nonlinear time history analyses, the following conclusions are drawn:

- As shown in the nonlinear time history analysis results, when the LRB is modeled as bilinear model, the axial demand from dynamic analysis is close to the estimated demand calculated using equivalent static force procedure presented in Session 2.
- If the axial demand of the LRB is obtained directly from the equivalent static design load or time history analysis using bilinear model, the base isolated building could have high probability of failure.
- As the isolation period increases, the probability of failure decreases accordingly.
- A simple amplification factor of 2.5 is proposed to increase the required axial capacity of the LRB (when the demand is calculated from the bilinear model) so as to ensure the probability of failure of the isolated building is within 10%.

- Subduction earthquakes dominate the failure of isolated buildings according to the analysis. For sites that are influenced by subduction hazard such as Vancouver, it is crucial to include subduction ground motions in the analyses.

7.2 Future Study

The recommendations for future study are listed as follows:

- The same procedure in this research can be repeated in case study of buildings with different height, and buildings with irregular shape, which will expand the spectrum and provide more comprehensive recommendations on LRB design.
- The failure criteria used in this study is simplified and conservative, a more realistic and detailed failure criterion can be proposed in the future study.
- The future study may also utilize the robust LRB model in OpenSees to investigate the effect of other LRB properties such as nonlinear tension behavior and lead degradation.

Bibliography

[1] G. P. Warn and K. L. Ryan, "A review of seismic isolation for buildings: historical development and research needs," *Buildings,* vol. 2, pp. 300-325, 2012.

[2] W. Robinson and A. Tucker, "A lead-rubber shear damper," *Bull. New Zealand Natl. Soc. Earthquake Engrg,* vol. 4, pp. 251-259, 1976.

[3] J. Weisman and G. P. Warn, "Stability of elastomeric and lead-rubber seismic isolation bearings," *Journal of Structural Engineering,* vol. 138, pp. 215-223, 2012.

[4] F. Naeim and J. M. Kelly, *Design of seismic isolated structures: from theory to practice*: John Wiley & Sons, 1999.

[5] G. P. Warn and A. S. Whittaker, "A study of the coupled horizontal-vertical behavior of elastomeric and lead-rubber seismic isolation bearings," 2006.

[6] T. A. Morgan and S. A. Mahin, "The optimization of multi-stage friction pendulum isolators for loss mitigation considering a range of seismic hazard," in *14th World Conference on Earthquake Engineering*, 2008, pp. 11-0070.

[7] T. Fujita, "Seismic isolation of civil buildings in Japan," *Progress in Structural Engineering and Materials,* vol. 1, pp. 295-300, 1998.

[8] M. Çelebi, "Successful performance of a base-isolated hospital building during the 17 January 1994 Northridge earthquake," *The Structural Design of Tall and Special Buildings,* vol. 5, pp. 95-109, 1996.

[9] J. Sanchez, A. Masroor, G. Mosqueda, and K. Ryan, "Static and dynamic stability of elastomeric bearings for seismic protection of structures," *Journal of structural engineering,* vol. 139, pp. 1149-1159, 2012.

[10] J. A. Haringx, "On highly compressible helical springs and rubber rods, and their application for vibration-free mountings," *Philips Research Reports,* vol. 3, pp. 401-449, 1948.

[11] A. N. Gent, "Elastic stability of rubber compression springs," *Journal of Mechanical Engineering Science,* vol. 6, pp. 318-326, 1964.

[12] C. G. Koh and J. M. Kelly, "Effects of axial load on elastomeric isolation bearings," University of California, Berkeley UCB/EERC-86/12, 1987.

[13] C. G. Koh and J. M. Kelly, "Viscoelastic stability model for elastomeric isolation bearings," *Journal of Structural Engineering,* vol. 115, pp. 285-302, 1989.

[14] C. G. Koh and J. M. Kelly, "A simple mechanical model for elastomeric bearings used in base isolation," *International journal of mechanical sciences,* vol. 30, pp. 933-943, 1988.

[15] G. P. Warn, A. S. Whittaker, and M. C. Constantinou, "Vertical stiffness of elastomeric and lead–rubber seismic isolation bearings," *Journal of Structural Engineering,* vol. 133, pp. 1227-1236, 2007.

[16] I. G. Buckle and H. Liu, "Critical loads of elastomeric isolators at high shear strain," presented at the Proceedings of 3rd U.S.-Japan Workshop on Earthquake Protective Systems for Bridges, 1994.

[17] ASCE, *Minimum Design Loads for Buildings and Other Structures*: American Society of Civil Engineers, Reston, VA, 2010.

[18] AASHTO, *Guide specifications for seismic isolation design*: American Association of State Highways and Transportation Officials, Washington, DC, 2014.

[19] NRCC, *National Building Code of Canada 2015*: National Research Council of Canada, Ottawa, ON, 2015.

[20] CSA, *Canadian Highway Bridge Design Code*: Canadian Standards Association, Missisauga, ON, 2014.

[21] MHURD, *Code for seismic design of buildings GB 50011 - 2010*: Ministry of Housing and Urban-Rural Development, Beijing, China, 2010.

[22] M. Kumar. Computer Program ElastomericX, LeadRubberX, and HDR: User elements in OpenSees for analysis of elastomeric seismic isolation bearings under extreme loading. 2014. Available: http://opensees.berkeley.edu/wiki/index.php

[23] PEER. Open System for Earthquake Engineering Simulation (OpenSees). 2000.

[24] M. Kumar, "Seismic isolation of nuclear power plants using elastomeric bearings," PhD Dissertation, the University at Buffalo, State University of New York, 2015.

[25] P. Fajfar, "Capacity spectrum method based on inelastic demand spectra," *Earthquake engineering and structural dynamics,* vol. 28, pp. 979-994, 1999.

[26] X. Chen, T. Yang, and W. Shi, "Influence of isolation hysteresis on the seismic performance of isolated buildings," *Structural Control and Health Monitoring,* vol. 22, pp. 631-647, 2015.

[27] NRC. Seismic hazard deaggregation for site Vancouver (City Hall). 2016.

[28] M. Bruneau, C.-M. Uang, and S. R. Sabelli, *Ductile design of steel structures*: McGraw Hill Professional, 2011.

[29] CSA, *Design of steel structures*: Canadian Standards Association, Missisauga, ON, 2014.

[30] A. Schellenberg, T. Yang, and E. Kohama, "OpenSees navigator," ed, 2005.

[31] P. J. Sayani, E. Erduran, and K. L. Ryan, "Comparative response assessment of minimally compliant low-rise base-isolated and conventional steel moment-resisting frame buildings," *Journal of Structural Engineering,* vol. 137, pp. 1118-1131, 2010.

[32] J. Cassidy, G. Rogers, M. Lamontagne, S. Halchuk, and J. Adams, "Canada's earthquakes:'The good, the bad, and the ugly'," *Geoscience Canada*, vol. 37, 2010.

[33] CREW. Cascadia Subduction Zone Earthquakes: A magnitude 9.0 earthquake scenario. 2013. Available: http://crew.org/sites/default/files/cascadia_subduction_scenario_2013.pdf

[34] CREW. Cascadia Shallow Earthquakes. 2009. Available: http://crew.org/sites/default/files/CREWshallowFinalSmall.pdf

[35] CREW. Cascadia Deep Earthquakes. 2008. Available: http://crew.org/sites/default/files/CascDeepEQweb.pdf

[36] N. J. Balfour, "Sources of seismic hazard in British Columbia: what controls earthquakes in the crust?," PhD Dissertation, University of Victoria, 2011.

[37] K. Satake, K. Shimazaki, Y. Tsuji, and K. Ueda, "Time and size of a giant earthquake in Cascadia inferred from Japanese tsunami records of January 1700," *Nature*, vol. 379, pp. 246-249, 1996.

[38] NRC. Simplified seismic hazard map for Canada, the provinces and territories. 2017. Available: http://www.seismescanada.rncan.gc.ca/hazard-alea/simphaz-en.php

[39] B. F. Atwater, S. Musumi-Rokkaku, K. Satake, Y. Tsuji, K. Ueda, and D. K. Yamaguchi, *The orphan tsunami of 1700: Japanese clues to a parent earthquake in North America*: University of Washington Press, 2016.

[40] USGS. Cascadia earthquake sources. Available: https://geomaps.wr.usgs.gov/pacnw/pacnweq/pdf/subd_eqpg.pdf

[41] J. W. Baker, "An introduction to probabilistic seismic hazard analysis," *Report for the US Nuclear Regulatory Commission, page Version*, vol. 1, 2008.

[42] S. Halchuk and J. Adams, "Deaggregation of seismic hazard for selected Canadian cities," presented at the Proceedings of the 13th World Conference on Earthquake Engineering, Vancouver, Canada. Paper, 2004.

[43] M. A. Galaviz Gonzalez, "Seismic response of tall buildings using ground motions based on National Building Code Canada 2015," Master Thesis, University of British Columbia, 2017.

[44] S. Halchuk, T. Allen, J. Adams, and G. Rogers, "Fifth generation seismic hazard model input files as proposed to produce values for the 2015 National Building Code of Canada," *Geol. Surv. Canada Open File*, vol. 7576, p. 15, 2014.

[45] T. I. Allen, J. Adams, and S. Halchuk, "The seismic hazard model for Canada: Past, present and future," presented at the Proceedings of the Tenth Pacific Conference on Earthquake Engineering, 2015.

[46] G. M. Atkinson and J. Adams, "Ground motion prediction equations for application to the 2015 Canadian national seismic hazard maps," *Canadian Journal of Civil Engineering*, vol. 40, pp. 988-998, 2013.

[47] PEER. NGA-West2 -- Shallow Crustal Earthquakes in Active Tectonic Regimes. 2013.

[48] A. Bebamzadeh, C. Ventura, and M. Fairhurst. S2GM: Tool for Selection and Scaling of Ground Motions. 2015.

Appendices

Appendix A LRB Geometric Properties

Table A.1 LRB geometric properties (Building A – $3T_f$ – t_r = 3mm)

Building A - $3T_f$ - t_r = 3mm											
Type A				Type B				Type C			
D_1	D_2	n_r	Amplification factor	D_1	D_2	n_r	Amplification factor	D_1	D_2	n_r	Amplification factor
[m]	[m]	[-]	[-]	[m]	[m]	[-]	[-]	[m]	[m]	[-]	[-]
0.142	0.282	8	1.15	0.100	0.292	11	1.12	0.071	0.295	12	1.14
0.142	0.295	9	1.31	0.100	0.303	12	1.26	0.071	0.306	13	1.28
0.142	0.319	11	1.61	0.100	0.325	14	1.52	0.071	0.328	15	1.56
0.142	0.331	12	1.76	0.100	0.345	16	1.79	0.071	0.348	17	1.84
0.142	0.353	14	2.05	0.100	0.364	18	2.04	0.071	0.367	19	2.12
0.142	0.373	16	2.32	0.100	0.383	20	2.29	0.071	0.376	20	2.26
0.142	0.393	18	2.58	0.100	0.400	22	2.53	0.071	0.394	22	2.53
0.142	0.411	20	2.83	0.100	0.417	24	2.77	0.071	0.411	24	2.80
0.142	0.429	22	3.06	0.100	0.441	27	3.11	0.071	0.427	26	3.07
0.142	0.446	24	3.29	0.100	0.456	29	3.33	0.071	0.443	28	3.33
0.142	0.462	26	3.51	0.100	0.471	31	3.55	0.071	0.458	30	3.58
0.142	0.486	29	3.83	0.100	0.485	33	3.76	0.071	0.473	32	3.83
0.142	0.501	31	4.03	0.100	0.506	36	4.06	0.071	0.487	34	4.08
0.142	0.523	34	4.32	0.100	0.519	38	4.26	0.071	0.501	36	4.32

Table A.2 LRB geometric properties (Building A – $3T_f - t_r$ = 9mm)

Building A - $3T_f$ - t_r = 9mm											
Type A				Type B				Type C			
D_1	D_2	n_r	Amplification factor	D_1	D_2	n_r	Amplification factor	D_1	D_2	n_r	Amplification factor
[m]	[m]	[-]	[-]	[m]	[m]	[-]	[-]	[m]	[m]	[-]	[-]
0.142	0.393	6	1.22	0.100	0.392	7	1.07	0.071	0.411	8	1.16
0.142	0.420	7	1.46	0.100	0.417	8	1.27	0.071	0.435	9	1.36
0.142	0.446	8	1.70	0.100	0.463	10	1.68	0.071	0.458	10	1.56
0.142	0.470	9	1.94	0.100	0.485	11	1.89	0.071	0.480	11	1.76
0.142	0.493	10	2.18	0.100	0.506	12	2.09	0.071	0.521	13	2.17
0.142	0.515	11	2.42	0.100	0.525	13	2.30	0.071	0.540	14	2.37
0.142	0.537	12	2.66	0.100	0.545	14	2.50	0.071	0.559	15	2.58
0.142	0.557	13	2.89	0.100	0.581	16	2.91	0.071	0.577	16	2.78
0.142	0.577	14	3.12	0.100	0.598	17	3.11	0.071	0.611	18	3.19
0.142	0.596	15	3.35	0.100	0.615	18	3.31	0.071	0.628	19	3.39
0.142	0.614	16	3.57	0.100	0.632	19	3.51	0.071	0.644	20	3.59
0.142	0.632	17	3.79	0.100	0.663	21	3.90	0.071	0.659	21	3.80
0.142	0.650	18	4.01	0.100	0.678	22	4.09	0.071	0.690	23	4.20
0.142	0.683	20	4.44	0.100	0.693	23	4.28	0.071	0.704	24	4.40

Table A.3 LRB geometric properties (Building A – $3T_f - t_r$ = 15mm)

Building A - $3T_f$ - t_r = 15mm											
Type A				Type B				Type C			
D_1	D_2	n_r	Amplification factor	D_1	D_2	n_r	Amplification factor	D_1	D_2	n_r	Amplification factor
[m]	[m]	[-]	[-]	[m]	[m]	[-]	[-]	[m]	[m]	[-]	[-]
0.142	0.454	5	1.14	0.100	0.463	6	1.06	0.071	0.494	7	1.18
0.142	0.493	6	1.42	0.100	0.499	7	1.29	0.071	0.527	8	1.40
0.142	0.530	7	1.69	0.100	0.532	8	1.52	0.071	0.559	9	1.62
0.142	0.564	8	1.98	0.100	0.593	10	1.98	0.071	0.588	10	1.84
0.142	0.596	9	2.26	0.100	0.621	11	2.22	0.071	0.617	11	2.06
0.142	0.596	9	2.26	0.100	0.648	12	2.45	0.071	0.644	12	2.29
0.142	0.626	10	2.54	0.100	0.673	13	2.69	0.071	0.670	13	2.52
0.142	0.655	11	2.82	0.100	0.698	14	2.92	0.071	0.719	15	2.97
0.142	0.683	12	3.09	0.100	0.722	15	3.16	0.071	0.742	16	3.20
0.142	0.710	13	3.37	0.100	0.745	16	3.39	0.071	0.765	17	3.43
0.142	0.736	14	3.64	0.100	0.768	17	3.62	0.071	0.787	18	3.66
0.142	0.760	15	3.91	0.100	0.790	18	3.85	0.071	0.808	19	3.89
0.142	0.784	16	4.18	0.100	0.811	19	4.09	0.071	0.829	20	4.11
0.142	0.808	17	4.45	0.100	0.832	20	4.31	0.071	0.849	21	4.34

Table A.4 LRB geometric properties (Building A – $4T_f - t_r$ = 3mm)

Building A - $4T_f$ - t_r = 3mm											
Type A				Type B				Type C			
D_1	D_2	n_r	Amplification factor	D_1	D_2	n_r	Amplification factor	D_1	D_2	n_r	Amplification factor
[m]	[m]	[-]	[-]	[m]	[m]	[-]	[-]	[m]	[m]	[-]	[-]
0.118	0.401	35	1.03	0.084	0.401	40	1.03	0.059	0.391	39	1.03
0.118	0.436	42	1.28	0.084	0.433	47	1.28	0.059	0.420	45	1.28
0.118	0.468	49	1.52	0.084	0.463	54	1.53	0.059	0.446	51	1.52
0.118	0.503	57	1.78	0.084	0.491	61	1.76	0.059	0.471	57	1.76
0.118	0.535	65	2.02	0.084	0.521	69	2.01	0.059	0.499	64	2.04
0.118	0.565	73	2.25	0.084	0.550	77	2.26	0.059	0.522	70	2.27
0.118	0.601	83	2.52	0.084	0.580	86	2.52	0.059	0.547	77	2.53
0.118	0.632	92	2.75	0.084	0.609	95	2.77	0.059	0.571	84	2.78

Table A.5 LRB geometric properties (Building A – $4T_f - t_r$ = 9mm)

Building A - $4T_f$ - t_r = 9mm											
Type A				Type B				Type C			
D_1	D_2	n_r	Amplification factor	D_1	D_2	n_r	Amplification factor	D_1	D_2	n_r	Amplification factor
[m]	[m]	[-]	[-]	[m]	[m]	[-]	[-]	[m]	[m]	[-]	[-]
0.118	0.503	19	1.04	0.084	0.510	22	1.02	0.059	0.518	23	1.04
0.118	0.550	23	1.32	0.084	0.553	26	1.27	0.059	0.561	27	1.30
0.118	0.583	26	1.53	0.084	0.594	30	1.53	0.059	0.591	30	1.50
0.118	0.625	30	1.81	0.084	0.631	34	1.78	0.059	0.628	34	1.76
0.118	0.654	33	2.01	0.084	0.667	38	2.03	0.059	0.664	38	2.03
0.118	0.692	37	2.27	0.084	0.700	42	2.28	0.059	0.698	42	2.29
0.118	0.727	41	2.53	0.084	0.732	46	2.52	0.059	0.730	46	2.55
0.118	0.761	45	2.77	0.084	0.763	50	2.76	0.059	0.761	50	2.81

Table A.6 LRB geometric properties (Building A – $4T_f - t_r$ = 15mm)

Building A - $4T_f$ - t_r = 15mm											
Type A				Type B				Type C			
D_1	D_2	n_r	Amplification factor	D_1	D_2	n_r	Amplification factor	D_1	D_2	n_r	Amplification factor
[m]	[m]	[-]	[-]	[m]	[m]	[-]	[-]	[m]	[m]	[-]	[-]
0.118	0.591	16	1.07	0.084	0.594	18	1.00	0.059	0.607	19	1.02
0.118	0.642	19	1.33	0.084	0.655	22	1.30	0.059	0.667	23	1.32
0.118	0.673	21	1.50	0.084	0.698	25	1.53	0.059	0.709	26	1.54
0.118	0.718	24	1.76	0.084	0.738	28	1.75	0.059	0.748	29	1.77
0.118	0.761	27	2.01	0.084	0.788	32	2.06	0.059	0.798	33	2.07
0.118	0.801	30	2.27	0.084	0.824	35	2.28	0.059	0.833	36	2.29
0.118	0.839	33	2.51	0.084	0.858	38	2.50	0.059	0.867	39	2.52
0.118	0.876	36	2.76	0.084	0.901	42	2.80	0.059	0.910	43	2.82

Table A.7 LRB geometric properties (Building A – $5T_f$ – t_r = 3mm)

Building A - $5T_f$ - t_r = 3mm											
Type A				Type B				Type C			
D_1	D_2	n_r	Amplification factor	D_1	D_2	n_r	Amplification factor	D_1	D_2	n_r	Amplification factor
[m]	[m]	[-]	[-]	[m]	[m]	[-]	[-]	[m]	[m]	[-]	[-]
0.107	0.531	101	1.00	0.075	0.516	106	1.01	0.053	0.493	98	1.01
0.107	0.584	123	1.25	0.075	0.561	126	1.26	0.053	0.532	114	1.26
0.107	0.636	147	1.51	0.075	0.605	147	1.50	0.053	0.570	131	1.51
0.107	0.687	172	1.76	0.075	0.650	170	1.76	0.053	0.605	148	1.76
0.107	0.738	199	2.01	0.075	0.692	193	2.00	0.053	0.641	166	2.01
0.107	0.789	228	2.26	0.075	0.735	218	2.25	0.053	0.674	184	2.26

Table A.8 LRB geometric properties (Building A – $5T_f$ – t_r = 9mm)

Building A - $5T_f$ - t_r = 9mm											
Type A				Type B				Type C			
D_1	D_2	n_r	Amplification factor	D_1	D_2	n_r	Amplification factor	D_1	D_2	n_r	Amplification factor
[m]	[m]	[-]	[-]	[m]	[m]	[-]	[-]	[m]	[m]	[-]	[-]
0.107	0.630	48	1.00	0.075	0.635	54	1.02	0.053	0.633	54	1.02
0.107	0.691	58	1.27	0.075	0.691	64	1.27	0.053	0.683	63	1.27
0.107	0.747	68	1.52	0.075	0.742	74	1.52	0.053	0.730	72	1.51
0.107	0.799	78	1.77	0.075	0.790	84	1.76	0.053	0.774	81	1.75
0.107	0.848	88	2.00	0.075	0.835	94	2.00	0.053	0.820	91	2.02
0.107	0.898	99	2.25	0.075	0.883	105	2.26	0.053	0.860	100	2.26

Table A.9 LRB geometric properties (Building A – $5T_f$ – t_r = 15mm)

Building A - $5T_f$ - t_r = 15mm											
Type A				Type B				Type C			
D_1	D_2	n_r	Amplification factor	D_1	D_2	n_r	Amplification factor	D_1	D_2	n_r	Amplification factor
[m]	[m]	[-]	[-]	[m]	[m]	[-]	[-]	[m]	[m]	[-]	[-]
0.107	0.721	38	1.01	0.075	0.730	43	1.00	0.053	0.737	44	1.01
0.107	0.792	46	1.28	0.075	0.803	52	1.28	0.053	0.801	52	1.26
0.107	0.849	53	1.51	0.075	0.862	60	1.52	0.053	0.860	60	1.51
0.107	0.910	61	1.77	0.075	0.917	68	1.77	0.053	0.915	68	1.77
0.107	0.967	69	2.03	0.075	0.969	76	2.01	0.053	0.967	76	2.02
0.107	1.021	77	2.28	0.075	1.024	85	2.28	0.053	1.017	84	2.27

Table A.10 LRB geometric properties (Building B – 1.5T_f – t_r = 3mm)

Building B - 1.5T_f - t_r = 3mm											
Type A				Type B				Type C			
D_1	D_2	n_r	Amplification factor	D_1	D_2	n_r	Amplification factor	D_1	D_2	n_r	Amplification factor
[m]	[m]	[-]	[-]	[m]	[m]	[-]	[-]	[m]	[m]	[-]	[-]
0.204	0.396	9	1.08	0.144	0.457	16	1.03	0.102	0.483	19	1.00
0.204	0.427	11	1.30	0.144	0.505	20	1.30	0.102	0.540	24	1.31
0.204	0.456	13	1.50	0.144	0.550	24	1.54	0.102	0.582	28	1.54
0.204	0.496	16	1.79	0.144	0.591	28	1.78	0.102	0.621	32	1.76
0.204	0.534	19	2.05	0.144	0.638	33	2.05	0.102	0.666	37	2.01
0.204	0.568	22	2.28	0.144	0.674	37	2.25	0.102	0.709	42	2.26
0.204	0.601	25	2.51	0.144	0.724	43	2.54	0.102	0.757	48	2.54
0.204	0.642	29	2.79	0.144	0.764	48	2.76	0.102	0.795	53	2.76
0.204	0.681	33	3.05	0.144	0.809	54	3.01	0.102	0.838	59	3.01
0.204	0.718	37	3.29	0.144	0.851	60	3.25	0.102	0.879	65	3.25

Table A.11 LRB geometric properties (Building B – 1.5T_f – t_r = 9mm)

Building B - 1.5T_f - t_r = 9mm											
Type A				Type B				Type C			
D_1	D_2	n_r	Amplification factor	D_1	D_2	n_r	Amplification factor	D_1	D_2	n_r	Amplification factor
[m]	[m]	[-]	[-]	[m]	[m]	[-]	[-]	[m]	[m]	[-]	[-]
0.204	0.521	6	1.03	0.144	0.610	10	1.04	0.102	0.658	12	1.00
0.204	0.590	8	1.42	0.144	0.665	12	1.28	0.102	0.733	15	1.30
0.204	0.622	9	1.60	0.144	0.716	14	1.52	0.102	0.780	17	1.50
0.204	0.652	10	1.79	0.144	0.764	16	1.76	0.102	0.845	20	1.80
0.204	0.709	12	2.15	0.144	0.830	19	2.10	0.102	0.905	23	2.09
0.204	0.735	13	2.32	0.144	0.871	21	2.32	0.102	0.943	25	2.28
0.204	0.786	15	2.66	0.144	0.911	23	2.53	0.102	0.998	28	2.56
0.204	0.810	16	2.82	0.144	0.967	26	2.84	0.102	1.049	31	2.83
0.204	0.856	18	3.14	0.144	1.003	28	3.04	0.102	1.082	33	3.01
0.204	0.878	19	3.29	0.144	1.054	31	3.33	0.102	1.130	36	3.27

Table A.12 LRB geometric properties (Building B – $1.5T_f - t_r$ = 15mm)

Building B - $1.5T_f - t_r$ = 15mm											
Type A				Type B				Type C			
D_1	D_2	n_r	Amplification factor	D_1	D_2	n_r	Amplification factor	D_1	D_2	n_r	Amplification factor
[m]	[m]	[-]	[-]	[m]	[m]	[-]	[-]	[m]	[m]	[-]	[-]
0.204	0.652	6	1.20	0.144	0.740	9	1.10	0.102	0.809	11	1.07
0.204	0.699	7	1.43	0.144	0.816	11	1.39	0.102	0.879	13	1.30
0.204	0.744	8	1.66	0.144	0.851	12	1.53	0.102	0.943	15	1.53
0.204	0.786	9	1.88	0.144	0.917	14	1.81	0.102	1.003	17	1.76
0.204	0.825	10	2.10	0.144	0.979	16	2.09	0.102	1.087	20	2.10
0.204	0.863	11	2.32	0.144	1.037	18	2.37	0.102	1.140	22	2.33
0.204	0.899	12	2.54	0.144	1.065	19	2.50	0.102	1.190	24	2.55
0.204	0.934	13	2.75	0.144	1.119	21	2.77	0.102	1.239	26	2.77
0.204	1.000	15	3.17	0.144	1.170	23	3.03	0.102	1.308	29	3.10
0.204	1.032	16	3.37	0.144	1.219	25	3.28	0.102	1.352	31	3.31

Table A.13 LRB geometric properties (Building B – $2T_f - t_r$ = 3mm)

Building B - $2T_f - t_r$ = 3mm											
Type A				Type B				Type C			
D_1	D_2	n_r	Amplification factor	D_1	D_2	n_r	Amplification factor	D_1	D_2	n_r	Amplification factor
[m]	[m]	[-]	[-]	[m]	[m]	[-]	[-]	[m]	[m]	[-]	[-]
0.177	0.565	40	1.01	0.125	0.620	56	1.00	0.089	0.635	60	1.00
0.177	0.625	50	1.25	0.125	0.691	70	1.25	0.089	0.704	74	1.26
0.177	0.691	62	1.51	0.125	0.763	86	1.51	0.089	0.771	89	1.51
0.177	0.751	74	1.75	0.125	0.830	102	1.75	0.089	0.837	105	1.76
0.177	0.815	88	2.01	0.125	0.898	120	2.00	0.089	0.901	122	2.01

Table A.14 LRB geometric properties (Building B – $2T_f - t_r$ = 9mm)

Building B - $2T_f$ - t_r = 9mm											
Type A				Type B				Type C			
D_1	D_2	n_r	Amplification factor	D_1	D_2	n_r	Amplification factor	D_1	D_2	n_r	Amplification factor
[m]	[m]	[-]	[-]	[m]	[m]	[-]	[-]	[m]	[m]	[-]	[-]
0.177	0.696	21	1.03	0.125	0.780	30	1.03	0.089	0.825	34	1.01
0.177	0.756	25	1.25	0.125	0.853	36	1.27	0.089	0.905	41	1.25
0.177	0.824	30	1.52	0.125	0.931	43	1.53	0.089	0.988	49	1.53
0.177	0.887	35	1.76	0.125	1.002	50	1.78	0.089	1.056	56	1.76
0.177	0.946	40	2.00	0.125	1.069	57	2.02	0.089	1.129	64	2.01

Table A.15 LRB geometric properties (Building B – $2T_f - t_r$ = 15mm)

Building B - $2T_f$ - t_r = 15mm											
Type A				Type B				Type C			
D_1	D_2	n_r	Amplification factor	D_1	D_2	n_r	Amplification factor	D_1	D_2	n_r	Amplification factor
[m]	[m]	[-]	[-]	[m]	[m]	[-]	[-]	[m]	[m]	[-]	[-]
0.177	0.802	17	1.03	0.125	0.898	24	1.00	0.089	0.982	29	1.02
0.177	0.887	21	1.31	0.125	1.002	30	1.29	0.089	1.078	35	1.27
0.177	0.946	24	1.52	0.125	1.081	35	1.53	0.089	1.166	41	1.52
0.177	1.019	28	1.78	0.125	1.155	40	1.77	0.089	1.248	47	1.77
0.177	1.087	32	2.04	0.125	1.238	46	2.04	0.089	1.325	53	2.01

Table A.16 LRB geometric properties (Building B – $2.5T_f - t_r$ = 3mm)

Building B - $2.5T_f$ - t_r = 3mm											
Type A				Type B				Type C			
D_1	D_2	n_r	Amplification factor	D_1	D_2	n_r	Amplification factor	D_1	D_2	n_r	Amplification factor
[m]	[m]	[-]	[-]	[m]	[m]	[-]	[-]	[m]	[m]	[-]	[-]
0.155	0.756	119	1.00	0.110	0.793	146	1.00	0.077	0.786	145	1.01
0.155	0.851	152	1.25	0.110	0.890	185	1.25	0.077	0.875	180	1.25
0.155	0.946	189	1.50	0.110	0.987	228	1.50	0.077	0.962	218	1.50
0.155	1.041	230	1.76	0.110	1.085	276	1.75	0.077	1.050	260	1.75
0.155	1.134	274	2.00	0.110	1.182	328	2.00	0.077	1.139	306	2.01

Table A.17 LRB geometric properties (Building B – 2.5T_f – t_r = 9mm)

Building B - 2.5T_f - t_r = 9mm											
Type A				Type B				Type C			
D_1	D_2	n_r	Amplification factor	D_1	D_2	n_r	Amplification factor	D_1	D_2	n_r	Amplification factor
[m]	[m]	[-]	[-]	[m]	[m]	[-]	[-]	[m]	[m]	[-]	[-]
0.155	0.869	53	1.01	0.110	0.941	69	1.01	0.077	0.977	75	1.01
0.155	0.967	66	1.26	0.110	1.043	85	1.26	0.077	1.082	92	1.26
0.155	1.056	79	1.50	0.110	1.142	102	1.51	0.077	1.177	109	1.51
0.155	1.150	94	1.76	0.110	1.237	120	1.76	0.077	1.265	126	1.75
0.155	1.242	110	2.01	0.110	1.331	139	2.01	0.077	1.357	145	2.00

Table A.18 LRB geometric properties (Building B – 2.5T_f – t_r = 15mm)

Building B - 2.5T_f - t_r = 15mm											
Type A				Type B				Type C			
D_1	D_2	n_r	Amplification factor	D_1	D_2	n_r	Amplification factor	D_1	D_2	n_r	Amplification factor
[m]	[m]	[-]	[-]	[m]	[m]	[-]	[-]	[m]	[m]	[-]	[-]
0.155	0.984	41	1.01	0.110	1.083	55	1.02	0.077	1.146	62	1.01
0.155	1.084	50	1.25	0.110	1.194	67	1.27	0.077	1.260	75	1.26
0.155	1.185	60	1.51	0.110	1.296	79	1.50	0.077	1.373	89	1.51
0.155	1.279	70	1.76	0.110	1.398	92	1.75	0.077	1.476	103	1.77
0.155	1.374	81	2.02	0.110	1.499	106	2.01	0.077	1.573	117	2.01